Università degli Studi di Padova

Dipartimento di Ingegneria Industriale
Corso di Laurea in Ingegneria Meccanica

Tesi di Laurea Magistrale

Effect of damping in VIV energy harvesting devices

Relatore:
Prof. Francesco De Vanna

Laureando:
Umberto Pavan

Correlatore:
Prof. Giovanna Cavazzini

Anno accademico 2023 / 2024

A mio nonno Antonio

Riassunto

Le fonti di energia rinnovabile stanno acquisendo sempre maggiore importanza, in questo ambito i VIV energy harvester possono giocare un ruolo importante nello sfruttamento delle cosiddette micro-hydro. In questo contesto nasce questo studio che si prefigge come obiettivo la delineazione di linee guida, rispetto allo smorzamento meccanico, per la progettazione degli energy harvester VIV Lo studio consiste nell'analisi di due configurazioni, una con un corpo cilindrico come corpo oscillante e l'altra con un prisma a base quadrata. Lo studio è stato seguito tramite simulazioni unsteady RANS bidimensionali. Si vogliono osservare gli effetti dello smorzamento sull'interazione tra fluido e sistema meccanico in configurazione open stream cross-flow.

La struttura ed i contenuti di questa tesi vengono riassunti di seguito:

- Il capitolo 1 consiste in una breve presentazione del contesto dello studio insieme a una rassegna dei contenuti disponibili in letteratura riguardanti il fenomeno delle scie vorticose, il suo studio in ambito ingegneristico per poi soffermarsi maggiormente sugli studi legati allo sfruttamento delle vibrazioni indotte da vortici.

- Il capitolo 2 contiene una descrizione fisica del fenomeno della formazione delle scie vorticose, indicando i parametri di riferimento rispetto a questo fenomeno, quali il numero di Reynolds e il numero di Stourhal. Di seguito viene illustrato il modello meccanico adottato per questo studio, all'interno del quale vengono presentati tutti i parametri che regolano il moto del corpo oscillante. Vi è poi un paragrafo dedicato alla dettagliata descrizione del setup numerico e computazionale. Le simulazioni sono state eseguite tramite ANSYS Fluent; il setup del sofrtware viene descritto nel dettaglio argomentando le scelte effettuate, in particolare, riguardo lo schema risolutivo adottato, le condizioni al contorno, la caratterizzazione della mesh dinamica e la definizione di una UDF necessaria per introdurre lo smorzamento nel modello. Il capitolo si conclude con un paragrafo dedicato alla discussione delle variabili che caratterizzano il modello; si evidenzia la suddivisione dello studio in due macrogruppi. Per il primo viene mantenuta costante la vera e propria rigidezza adimensionale del sistema, mentre per il secondo gruppo viene

mantenuto costante il parametro k^*, rappresentativo della rigidezza ma appositamente definito per avere particolari caratteristiche, tra le quali garantire la costanza di ρ.

- Il capitolo 3 riguarda il caso a sezione circolare. Vi è la descrizione e l'analisi della mesh adottata per questo caso, seguita da un breve paragrafo riguardante la convergenza delle simulazioni. Dopodiché vi è un paragrafo dedicato all'analisi dinamica che comprende l'illustrazione e la discussione dei risultati ottenuti. Viene descritto il comportamento del corpo oscillante in questa configurazione, evidenziando la concordanza dei risultati ottenuti con le informazioni reperibili in letteratura. I risultati delle simulazioni vengono esposti separatamente per i due gruppi di simulazioni presentati al capitolo precedente. Per ciascuno vengono analizzati tramite uno studio delle frequenze di oscillazione, delle ampiezze e dei valori di potenza al variare della velocità del flusso incidente e del rapporto di smorzamento.

- Il capitolo 4 riguarda il caso a sezione quadrata. Inizia con la presentazione delle differenze, sia del modello meccanico sia del setup numerico, rispetto a quello con sezione circolare A questo segue la presentazione della mesh utilizzata. La presentazione dei risultati inizia con la descrizione del comportamento tipico mantenuto dal prisma, evidenziando l'assenza di sincronia tra le oscillazioni del corpo e il distacco dei vortici. La medesima analisi dei risultati proposta per il cilindro viene fatta anche per questo caso.

- Il capitolo 5 contiene un riassunto delle conclusioni tratte da questo studio. In breve lo studio evidenzia una netta differenza di comportamento tra cilindro e prisma a base quadrata. Il moto del corpo cilindrico rispetta l'andamento atteso per le vibrazioni che hanno come causa il "vortex shedding". Presenta infatti una zona di sincronia limitata sia inferiormente che superiormente e da valori di potenza considerevoli solo per un range di velocità specifiche. Il prisma a base quadrata invece si oscilla in maniera non sincrona con i vortici che si distaccano, il suo comportamento è tipico delle vibrazioni "wind galloping". Il regime di funzionamento in questa configurazione è a velocità più elevate rispetto al precedente caso. Inoltre le potenze prodotte si mantengono all'incirca costanti per un ampio range di velocità.

SUMMARY

Renewable energy sources are becoming increasingly important, and in this context, VIV energy harvesters can play a relevant role in the exploitation of the so-called micro-hydro resources. This is the background of this study, which aims to outline guidelines, concerning mechanical damping, for the design of VIV energy harvesters.
The study analyses two configurations, one with a circular cross-section and the other with a squared cross-section, performed using unsteady bi-dimensional RANS. The effects of damping on the interaction between fluid and mechanical system in an open-stream cross-flow configuration are to be observed.

The structure of this thesis is as follows:

- **Chapter 1** 1 consists of a brief presentation of the context of the study together with a literature review describing some of the studies carried out in the field and the state of the art regarding VIV energy harvesters.

- **Chapter 2** contains a physical description of the phenomenon of vortex street formation, followed by an illustration of the mechanical model adopted for this study. This section contains a paragraph dedicated to the detailed presentation of the numerical and computational setup and concludes with a focus on the variables characterising the model.
- **Chapter 3** relates to the circular section case. A short paragraph concerning the convergence of the simulations follows a description and analysis of the mesh adopted for this case. The following section is devoted to the dynamic analysis, which includes the illustration and discussion of the results obtained for all the configurations of the cylindrical case.

- **Chapter 4** relates to the case with a square cross-section. It begins presenting the model's differences from the circular cross-section model, and then focuses on the description of the mesh used. The results obtained from the dynamic analysis are then presented and discussed.

- **Chapter 5** contains a summary of the conclusions drawn from this study.

Nomenclature

D $[m]$	Inflow flow velocity
U_∞ $[m/s]$	Inflow flow velocity
St $[-]$	Strouhal number
f_v $[Hz]$	Vortex shedding frequency
f_n $[Hz]$	Natural frequency of the spring-mass system
f_y $[Hz]$	y-translation frequency
m_0 $[Kg]$	Reference mass
h $[m]$	Cylinder length
m $[Kg]$	Cylinder mass
k $[N/m]$	Spring stiffness constant
k_0 $[N/m]$	Reference Spring stiffness constant
k^* $[N/m]$	Adimensional spring stiffness
y $[m]$	y-translation
y^* $[-]$	Adimensional y-translation
ρ_s $[Kg/m^3]$	Density of the cylinder material
ρ_f $[Kg/m^3]$	Density of the fluid
ρ_∞ $Kg/m^3]$	Density of the fluid
ρ^* $[-]$	Cylinder/flow ratio
μ_∞ $[-]$	Dynamic viscosity
Re $[-]$	Reynolds number
U_r $[-]$	Reduced velocity
St_y $[-]$	Adimensional y-translation frequency
ζ $[-]$	Damping ratio
P^* $[-]$	Adimensional mechanical power
L $[N]$	Lift force acting on the cross-section
$\dot{y}$ $[m/s]$	Cross-flow translation velocity
$\ddot{y}$ $[m/s^2]$	Cross-flow translation acceleration
L $[m]$	characteristic length of the cross-section

CONTENTS

- I -

Introduction

In recent years, there has been an increasing interest in the energetic field, mainly due to the economic and industrial growth of emerging nations and the need of shifting energy production from fossil sources to renewable or low-emission sources.
Implementing this energy transition means facing several challenging problems, including issues related to the intermittency in the energy production of renewable sources, particularly solar power plants and wind farms.
Compared to other renewable energy sources, hydropower provides greater stability and consistency in production, almost comparable to that of classic natural gas or coal-fired power plants. However, hydro resources with suitable characteristics for constructing power plants are relatively saturated. For this reason, it has become necessary to exploit also those sources in respect of which it is not convenient to undertake the high investments of conventional hydropower solutions. Smaller scale resources, or resources placed in areas where dams cannot be built, due to the conformation of the soil or the related geological risk, could still be exploited with other innovative solutions. Conventional hydropower plants, in fact, are currently only exploitable where it is possible to generate power outputs of at least 12-15kW and thus leave many potential smaller resources untapped. In this area, it is opportune to find types of plants that can be competitive despite the lower power outputs involved.

Energy harvesters are a significant innovation in this field. These devices are able to extract energy from fluid flows differently from conventional turbines. In fact, they derive energy from the phenomenon of vortex-induced vibration (VIV). This phenomenon takes place under certain determinate conditions, such as when a vortical wake (Von Karman vortex street) is formed downstream of a bluff body, which is invested by a fluid flow. The vortices in the wake alternately detach from the body, resulting in an alteration of the pressure field around the body, which, if it is free to move, is subject to oscillatory motion. The mechanical energy of the oscillatory motion can then be converted into electrical energy. Usually, these devices use piezoelectric crystals or electromagnetic generators capable of converting the energy of the motion.

The existence of vortex-induced vibrations has been well-known for a long time in the engineering field. In fact, this type of vibration is considered dangerous in most engineering applications because it can lead to excessive amplitude vibrations and to the collapse of structures such as bridges, transmission lines, aircraft control surfaces and many others.

However, this phenomenon can also be used to extract energy from the flow by coupling the bluff body to an electric generator or a piezoelectric crystal. To achieve good performance when using VIV energy harvesters, it is necessary to have a deeper understanding and knowledge of the motion of the bluff body. For example, what are the configurations for which energy harvesters are most effective in collecting energy? Given a particular configuration, how do energy harvesters behave when the parameters controlling the motion, such as stiffness, damping or density ratio of the system, vary? For some time now, VIV energy harvesters have been attracting some interest, and literature studies have provided answers to some of the above questions.

Starting from the concepts behind the phenomenon, many studies have been conducted with the aim of understanding the causes and behaviour of vortex streets, studying stationary bluff bodies, mainly cylinders, invested by a fluid flow. In 1980, Friehe (1980) conducted a study focusing on the detachment frequency of vortexes downstream of a cylinder to provide quantitative data on the relationship between Stourhal and Reynolds numbers. Subsequently, Achenbach and Heinecke (1981), maintaining the stationary cylinder configuration, investigated the effects of roughness on vortex shedding by conducting an experimental study involving flow analysis for a cylinder inside a wind tunnel; they found that surface roughness influences the Stourhal number in the critical regime, causing it to increase compared to the case with a smooth cylinder. Maintaining the focus on stationary cylinders, Triantafyllou et al. (1986) focused their study on the cause of vortex formation downstream of the cylinder by combining experimental studies with equations based on the inviscid fluid hypothesis. These studies provide valuable information on the physical principles governing vortex trails and are a good starting point for understanding the pivotal mechanisms of vortex-induced vibrations.

More specific information on this phenomenon can also be found in the literature by consulting those studies interested in the containment of vortex-induced vibrations since these can be a danger to structures. In particular, there are interesting studies concerning marine riser applications. In this area, Ding et al. (2004) conducted a study simulating at a riser-scale Reynolds number on smooth cylindrical bodies of various roughness and streaked cylindrical bodies, both in a cross-flow configuration. This study revealed a marked difference between smooth and streaked cylinders. According to Ding, oscillations as large as two diameters can occur for smooth cylinders, whereas for streaked cylinders, the vortex wake is almost absent, as is the induced oscillation. In 2006, Constantinides and Oakley (2006) conducted a study to develop a numerical model to predict the phenomenon in the same sector, but with a numerical approach based on RANS and DES (Detached Eddy Simulation).

Turning the focus to studies conducted on energy harvesters, a variety of information is available in the literature. Studies in this field assume different approaches, either emphasising the VIV phenomenon or researching configurations capable of extracting more power.
In this area, Goswami et al. (1993) conducted an experimental study on a cylinder mounted on springs in a wind tunnel; he investigated the effects of certain control variables of the system, including mechanical damping, which seems to have a certain relevance in the range of speeds at which the lock-in condition is maintained. Blackburn and Henderson (1996) then conducted a numerical analysis using a two-dimensional approach in a cross-flow configuration for one cylinder. The study clarified that the numerical method is an alternative to the experimental setup.
Maintaining the cross-flow configuration, Fu et al. (2013) experimentally investigated the behaviour of a flexible cylinder in a specific velocity range by subjecting it to both steady and oscillatory flows; this study exposed relevant differences concerning hysteresis and amplitude of oscillations depending on the type of incident flow. Remaining in the area of flexible cylinders, an interesting study conducted by Singh et al. (2012) approaches the problem by developing a bi-seismic mathematical model to describe the oscillations of a flexible cylinder.

Concerning power generation, a widely used approach for the conversion of mechanical energy is the use of piezoelectric crystals. In this area, Molino-Minero-Re et al. (2012) conducted a study with an energy harvester using a piezoelectric crystal connected to a cantilever as a voltage generator; the study also revealed a decrease in oscillation frequency as the diameter of the cylindrical body increased. Also, Wang et al. (2021), again exploiting

piezoelectric materials, studied a particular configuration involving the positioning of a rectangular plate downstream of the cylinder in order to extend the range of speeds at which the harvester is able to generate energy. His studies, which were carried out experimentally in wind tunnels, have shown that this configuration can better harness the power of the vortex wake.
Another interesting configuration was studied by Badhurshah et al. (2019), which involves mounting the cylinder on a bi-stable spring, again in order to extend the range of speeds for which the lock-in is maintained; they found out that the non-linearity of the spring is quite effective in pursuing this aim.
There are also other interesting approaches to the problem of VIVs, e.g. Raissi et al. (2019) conducted a study that exploited deep natural networks that encode the dynamic motion equation for the structure along with the incompressible Navier-Stokes equations to predict the velocity and pressure fields around the copes; these results can then be exploited in control applications.

Although a number of researches has been carried out on the VIV phenomenon and a great amount of information i available in the literature dealing with this topic, no clear guidelines can be identified for developing an energy harvester from start to finish. Therefore, the need arises to conduct studies that maintain simple configurations and can provide valid information in most cases.

The current study arises within the framework of the H-HOPE project, a European project that aims to identify the untapped potential of hydropower resources in the EU and develop technologies capable of exploiting hidden hydro. To this end, it seeks to develop an innovative technology capable of exploiting VIVs.

As can be seen from the 1.1, there are several harvester configurations proposed in this project:

- Piping
- Open stream
- Open channel

This study focuses on the open-stream cross-flow configuration with a

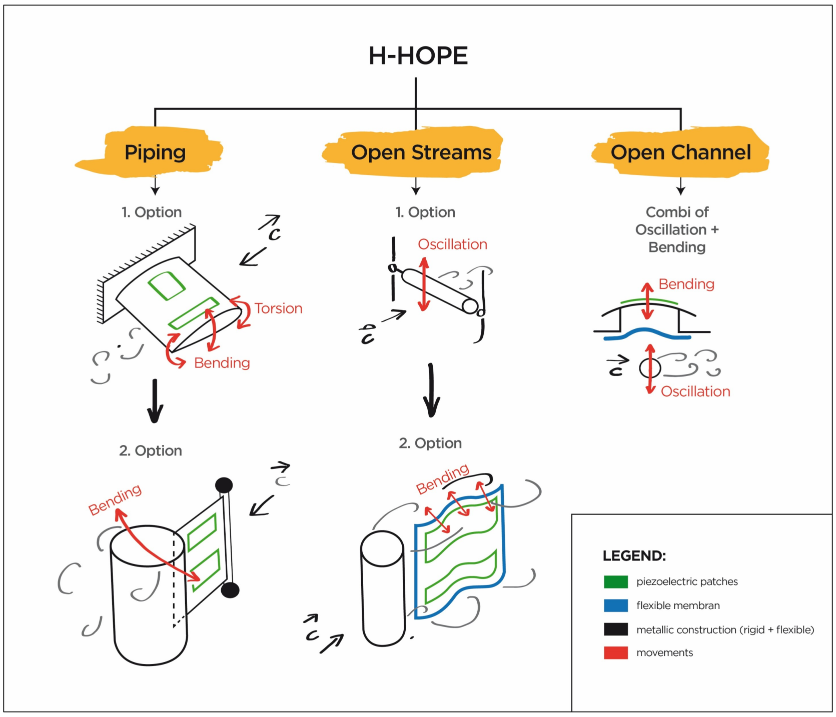

Figure 1.1: *Energy harvester configurations studied within the H-HOPE project.*

simple oscillating body; among the proposed configurations, it is probably the most studied due to its simplicity, and, for this reason, it is suitable for the purpose of deriving results of broader applications. Among the various areas available in this configuration, the focus is on the effect of the system's mechanical damping on the interaction between fluid and oscillating body. It aims to provide general guidelines regarding this parameter in VIV systems. In carrying out the study, a two-dimensional model was adopted, on which numerical analyses were conducted using Computational Fluid Dynamics (CFD), building a database of results.

Two different geometric configurations were adopted for this study, the first using a cylindrical body and the second using a square-based prism. On the one hand the configuration with the cylinder was chosen because it is the one which is mostly dealt with in the literature and, in any case, it gives good results in terms of energy collection. On the other hand, the second configuration, was chosen because, from preliminary studies, it appears to have good performance in different velocity ranges than those optimal for the cylinder, and could therefore be useful in exploiting resources that cannot be used with the first configuration.

- II -

Model definition and setup

In this chapter, everything concerning the approach to the problem is presented, both from an analytical point of view and from the point of view of the computational setup. In both cases, in order to avoid continual repetition, reference is always made to the case of the cylinder with a circular base throughout the length of the chapter. Note that the approach adopted for the case of the square-base prism is entirely similar to that of the cylindrical case; the few differences present will be highlighted in the chapter devoted to the square case.

Focusing now on the phenomenon of wake vortex formation, different behaviour can be observed depending on the value of the Reynolds number. In the study of bluff bodies interaction with fluid flows, cylindrical bodies are by far the most studied, so the next few lines, based on the literature, will describe the behaviour of a generic cylindrical body interacting with a fluid current.

For a given cylinder transversely crossed by a fluid flow, wakes of different shapes can be observed depending on the speed of the flow, since the Reynolds number and the speed are linked by the following relationship:

$$Re = \rho_\infty D U_\infty / \mu_\infty \qquad 2.1$$

According to Pantazopoulos (1994), if the surface of the cylinder is smooth, the following behaviour can be observed: if the Reynolds number is less than 5, the boundary layer is completely attached; as the Reynolds number increases between 5 and 40, two symmetrical delta vortices form downstream of the cylinder due to the separation of the boundary layer. As the Reynolds number increases in a range between 40 and 150, two regimes, in which vortex street is laminar, are observed. After a transition region between 150 and 300, a fully turbulent vortex street is reached for Reynolds numbers up to $3 \cdot 10^5$, this last region is called "subcritical". For even higher values of Reynolds number, a transition region is reached where the boundary layer becomes turbulent, causing a drastic drop in the drag coefficient. For Reynolds numbers higher than $3.5 \cdot 10^6$, a vortex street with a turbulent cylindrical boundary layer is again observed and it persists up to 10^{11}.

However, the Reynolds number is not the only parameter controlling the behaviour of the wake; many other factors such as cylinder surface roughness and turbulence of the incident flow can influence it, in addition to which, when considering real applications, there are even other modifying factors such as end effects for finite length cylinders or the flexibility of the body. In this study it is always assumed that the cylinder surface is smooth, there is no turbulence in the incident flow, the cylinder is infinite in length and has infinite stiffness.

If we now look at the vortex shedding frequency, we can see that it's a key parameter for harvesting energy from the flow, because when it's equal to the natural frequency of the mechanical system, resonance conditions are reached. As reported in Vortex Shedding From Bluff Bodies in a Shear Flow: Griffin (1985), the periodic lift force is amplified in this condition.
The vortex shedding frequency is considered via the Strouhal number, which is closely related to the Reynolds number as it can be seen in figure 2.1

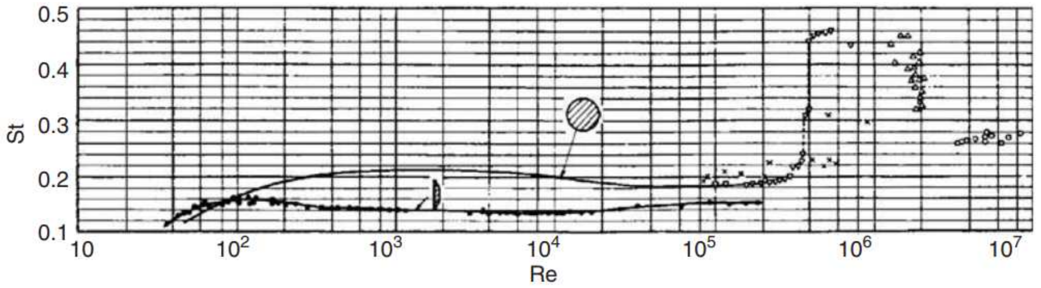

Figure 2.1: *Plot of Strouhal and Reynolds numbers for a circular cylinder. Experimental figure from Kaneko et al. (2008).*

The general formula for the Strouhal number is:

$$St = f_v D/U_\infty \tag{2.2}$$

where f_v is the vortex shedding frequency. When f_n is equal to f_v , the so-called "lock-in" condition is reached.

As De Vanna et al. (2023) report, the orthogonal displacement of the cylinder is considerably greater when the lock-in condition occurs, therefore more energy can be extracted from the flow in this condition.

Many other physical parameters such as density, stiffness, damping, etc. have a significant influence on the behaviour of the cylinder, so the next section will introduce the mechanical system of the case studied.

2.1 MECHANICAL MODEL DESCRIPTION

Since the objective of the current study is to investigate how the VIVs vary as the damping of the mechanical system varies and knowing that a large number of CFD simulations would be required to have a sufficiently large database, the mechanical system adopted is as simple as possible in order to reduce the computational time. Apart from that, note that the present study is part of the continuation of De Vanna et al. (2023)'s study and therefore adopts exactly the same mechanical model.

The mechanical system adopted consists in a 2D model in which the cylinder suspended in the fluid flow. The body is elastically suspended in the flow, with the height of the cylinder being perpendicular to the undisturbed flow direction, this is called a cross-flow configuration. Obviously the cylinder has a mass, the springs on which it is mounted aren't considered ideal, so they are characterised by stiffness and damping too. The cylinder can be displaced in the vertical direction, any other movement is not allowed, so the system has only one degree of freedom and is governed by the following differential equation:

$$m\ddot{\tilde{y}}(t) + c\dot{\tilde{y}} + k\tilde{y}(t) = F_y \tag{2.3}$$

where m is the mass of the cylinder, c is the damping of the springs, k is their stiffness and F_y is the resulting lift force on the cylinder. Furthermore $\tilde{y}$, $\dot{\tilde{y}}$, $\ddot{\tilde{y}}$ are verical displacement, velocity and acceleration respectively. In order to ensure that the results of the study are as general as possible, a non-dimensional formulation is adopted. It is obtained by normalising the parameters for a characteristic length and a characteristic time: D and U_∞/D respectively.

The physical quantities that are obtained are as follows:

$$y = \tilde{y}/D \qquad 2.4 \qquad\qquad t = \tilde{t}U_\infty/D \qquad 2.5$$

where y is the non-dimensional length and t is the non dimensional time. Equation 2.3 in the non-dimensional form becomes:

$$\rho A\ddot{y}/D^2 + \mu\dot{y} + \xi y = 2cy \qquad 2.6$$

which includes: the cylinder to fluid density ratio

$$\rho = \rho_s/\rho_\infty \qquad 2.7$$

the non-dimensional damping

$$\mu = c/(\rho_\infty U_\infty D) \qquad 2.8$$

the non-dimensional stiffness

$$\xi = k/(\rho_\infty U_\infty^2) \qquad 2.9$$

the lift coefficient

$$c_y = F_y/q_\infty \qquad 2.10 \qquad\qquad q_\infty = 1/(2\rho_\infty U_\infty^2 D) \qquad 2.11$$

While A/D^2 is only a geometric parameter resulting from the cylindrical shape chosen, ρ, μ, ξ are key parameters influencing the behaviour of the body. As De Vanna found out, different values of ρ significantly change both the speed range and the power output, so it was also expected that motion would be strongly dependent on the ξ and μ values. The choice of these values in this study was therefore crucial, as will be discussed later.

2.2 COMPUTATIONAL SETUP AND NUMERICAL METHODOLOGY

The present work was conducted using the commercial computational fluid dynamics platform ANSYS Fluent as the numerical reference solver, it has been used to solve the 2D Unsteady Reynolds-Averaged Navier-Stokes equations (URANS), it has been used to solve the Navier-Stokes equations which, given the incompressible nature of the problem that comes from the fact that the operating fluid is water, are reduced to just three equations: the continuity equation, the equation of conservation of momentum along the x-axis and the equation of momentum along the y-axis. The same equation along z-axis is not necessary since the problem is two-dimensional in the same way the energy equation is not implemented due to the incompressibility of the fluid.

Given the complexity of the problem and the need to run a significant number of simulations, within the H-Hope project a customised Python code was developed. This code can automatically edit a given journal file by entering into it the desired values for simulation parameters such as density, stiffness, fluid inlet velocity etc., which is all that's needed to set up the correct simulation. It can also generate appropriate commands within the journal file to implement a user-defined function (UDF) within a simulation; in short a UDF is a code defined outside of Fluent in which it is possible to create variables and mathematical functions that are not available in the main solver; more on UDFs will be discussed later. Finally, the code is capable of running simulations by entering the desired number of iterations in the journal file and generating the Slurm files which contain all the information required to run the simulations on Galileo100, such as the number of nodes desired to be used for the simulation, the memory allocation, which partition to use and all the information about the solver licence, the user and the project to which the simulation belongs.

It is important to emphasise that the simulations were conducted in the unsteady regime, taking into account the oscillating nature of the phenomenon under investigation. This approach made it possible to explore in detail system's behaviour over time, providing a complete and in-depth view of the phenomena at involved.

2.2.1 JOURNAL FILE

As mentioned earlier, the journal file contains all the information required by the ANSYS Fluent solver to perform an adequate simulation of the fluid field; this section describes in detail the contents of the journal file and explains the choices made during the study. The journal file is nothing more than a text file that can be summarised into nine sections:

- Mesh import
- Model definition
- Cell-zone conditions and boundary conditions definition
- Dynamic Mesh Characterisation
- User-defined Function Import
- Reference Values Set
- Solver Scheme Set
- Report Definition

Mesh import

The geometry to be simulated is imported into Fluent via a mesh file containing the mesh information described in the previous paragraph. To verify that the mesh has been imported correctly, a check command is given; this command corresponds, in Fluent's output file, called "fluentOut", to a section where it is possible to check various information about the imported mesh, such as domain extension, number of cells, number of nodes and others, to verify that there are no errors.

Model definition

The Models section defines the various settings to be used for the simulation, such as the type of algorithm to be implemented, the turbulence model and the type of fluid selected for the simulation.

The first decision to be made is whether to run a steady-state or a transient simulation. A steady-state simulation computes the fully developed solution that does not change over time, when a steady-state model is used the mean values are computed; this choice is appropriate when the flow field does not change significantly within time. Steady-state simulations are less expensive, in terms of computational cost, compared to transient simulations, but transient simulations are required when there is a time-dependent phenomenon of interest. The transient approach is best suited to simulate unsteady flows, such as turbulent flows, flow instabilities, transient events like start-up or shut-down processes and flow around moving objects, which happens to be the case in this study.

The second thing to choose is the algorithm to implement in the solution of the continuity and momentum equations.
Two approaches are available: density-based and pressure-based. Each provides several implementable options for solving the non-linear system governing fluid motion. The density-based approach solves the momentum continuity equations and, if necessary, energy and other equations simultaneously. This means that the non-linear equations are coupled and cannot be solved separately. The density-based calculation method linearises the non-linear system governing the motion in each mesh cell. This results in a linear system for each cell, the resolution of which provides updated values for the fluid field. The density-based approach provides two ways of linearising the equations of motion: an implicit way and an explicit way. In the implicit case, each unknown value in each cell corresponds to an equation containing both known values and unknowns values from neighbouring cells; therefore, each unknown value appears in several equations of the linear system, and they must be solved simultaneously. In contrast, in the explicit system, each unknown value in each cell is associated with an equation that contains only known values and can, therefore, be solved separately from the others. In summary, the implicit system solves for all variables in the whole mesh at the same time, whereas the explicit system solves for all variables one cell at a time. The explicit method is generally more accurate than the implicit method, but, since it uses information from the previous time step, the time step size must be limited to avoid the fluid travelling more than one cell per time step. This can result in a slower simulation and can be avoided using the implicit method.

The density-based solver is mainly recommended for high-speed compressible flows. This is because if the difference between the fluid velocity and the sound speed is minimal, which happens for low Mach numbers, the

Navier-Stokes equations, as they are written in the density-based approach, become (numerically) highly stiff. This also happens in incompressible fluids, where acoustic waves travel endlessly quickly regardless of the fluid velocity. Poor convergence rates are caused by the numerical stiffness of the equations. Fluent can overcome this problem by using a method known as preconditioning, but the density-based approach remains unrecommended for this study.

A better option for the current study is a pressure-based approach, which is recommended for incompressible or low-compressible flows. The pressure-based approach solves the non-linear system of equations governing the fluid flow by implementing an algorithm that comes from the projection method. In this method, the continuity equation is not solved directly. Instead, a so-called "pressure-correction" equation is solved. The pressure-correction equation comes from both the continuity and momentum equations, and it is used to correct the pressure so that the continuity is satisfied. As well as the density-based method, the pressure-based one comes in two forms: the coupled and segregated algorithms. The coupled algorithm solves simultaneously both the equations of momentum and the pressure-correction equation, more in detail it consists of the following steps:

1. Update the properties of the fluid based on the current solution;
2. Solve simultaneously the system of momentum and pressure-based continuity equation;
3. Update mass flux;
4. Solve energy equation (and others) if required;
5. Check if the solution converged;
6. End or iterate, depending on the convergence.

In contrast, the segregated method solves the governing equations segregated from one another; this means that each equation, while being solved, is decoupled from other equations. Since the equations aren't really segregated from one another in the non-linear system governing the fluid flow, the solution has to be calculated iteratively. Each iteration consists of the same steps followed by the coupled algorithm reported in the numbered list above, apart from step number two, which is split into two parts. In fact, the segregated algorithm solves each momentum equation sequentially first and then solves the pressure-correction equation for the continuity.
This last algorithm has a significantly lower rate of solution convergence

compared to the coupled algorithm; this happens because the equations are solved in a decoupled manner. On the other hand, the segregated approach is far more memory-efficient than the coupled algorithm because it only needs to store one equation in the memory at a time and not all of them together, as in the case of the coupled algorithm.
Both of these methods are suitable for the present study, but the segregated approach has been chosen because it provides a pressure-velocity coupling algorithm called “PISO”, which is recommended for the case of this study. More about the PISO algorithm will be discussed later in the journal file section.

The third thing to choose is the turbulence model. Turbulence models are needed to find unknown variables introduced in the equations to avoid the resolution of small scales, which are too computationally expensive to simulate. In fact, since the velocity fields are characterized by fluctuations of velocity, quantities such as momentum and energy result to be fluctuating also. These fluctuations can be of small scales at high frequency, and the simulation of these scales can not be performed either in a reasonable time or with limited computing resources. Instead, the equations are manipulated (removing the small scales or time-averaging them), resulting in equations that are cheaper to solve but contain the unknown variables mentioned earlier.
As will be mentioned in the paragraphs on meshes, three different turbulence models were tested in this study. k-ω SST was the one that performed best, so it has been chosen.
Even if it is impossible to establish an absolute hierarchy among the turbulence models, the k-w SST is an excellent choice for problems of this kind. Its effectiveness derives from the fact that it can exploit both the omega and epsilon. The following formula wants to be representative of this capability:

$$\omega \text{ equation} + \text{blend function} \times \epsilon \text{ equation} \qquad 2.12$$

Where the blend function assumes values close to zero near the wall, and therefore, the equation for W is exploited, while it assumes values equal to one far from the wall (far field), and consequently, the equation for epsilon is exploited.

The fourth and last thing to choose is material. A lot of physical properties may be defined for the material, such as density, viscosity, heat capacity, thermal conductivity and others.
In this case, the choice is pretty easy since the study aims to investigate the

behaviour of bluff bodies submerged in a water flow. The material has been copied from the Fluent library as “water-liquid”.

Cell-zone conditions and boundary conditions definition

In this section, two types of conditions are assigned to the control volume: cell-zone conditions and boundary conditions. The cell zone conditions cover the entire region in which the solver actually has to simulate the flow; this occurs in the whole domain, excluding the edges. On the other hand, boundary conditions are assigned to the edges of the control volume; through these, it is possible to impose the configuration of the motion to be simulated.

Cell zone conditions can be fluids or solids; in the present study, we want to simulate a water flow, so obviously, the condition will be fluid. A fluid zone consists of a group of cells in which all the equations governing motion are solved. It is also possible to specify other information, such as the presence of a source (of heat, mass, momentum, turbulence, etc.), a fixed value for a variable in the fluid zone, a zone in which the flow is simulated as laminar or a porous zone. It was not necessary to implement any of the above options during this study. Furthermore, if required, it is possible to specify a translating or rotating reference frame. In the case of this study, the reference frame is fixed. The fluid-cell-zone condition has been assigned to both the square region surrounding the cylinder and the rectangular zone outside the square visible in Figure 3.1.

As for boundary conditions, these must be assigned to the four outer sides of the mesh and the cylinder surface. The last is assigned the wall condition because the cylindrical surface is solid. It is possible to specify three settings within the wall condition: wall motion, shear condition and wall roughness. Regarding the wall motion, it has been excluded in the present study because, although the cylinder moves within the fluid field, there is no relative motion between fluid and cylindrical surface at the interface (as could be the case, for example, if a rotational motion around his axis was imposed to the cylinder). The shear condition at the interface is set as "no-slip,"this setting is the default in Fluent and dictates that the fluid and the wall must move with the same velocity meaning that the fluid has to stick to the wall. Finally, the surface roughness affects the wall-bounded flow, and Fluent takes this into account by changing the Law-of-the-wall. In this study, the roughness was simulated by keeping the default value proposed by Fluent for the roughness constant (0.5).

The sides limiting the control region above and below were assigned the symmetry condition. Although this is usually used to simulate geometries with mirror symmetry, in this case, it is used to model a wall with zero-shear slip. In fact, the symmetry condition imposes that there must be fields with no component orthogonal to the surface, as happens in the case of the wall boundary condition, but without imposing the no-slip condition. In the problem to be simulated in this study, the symmetry boundary condition turns out to be adequate because, although the control volume has no mirror symmetry with respect to the outer sides, it is assumed that the oscillatory motion of the cylinder does not affect the fluid velocity field in regions far away from the cylinder. Thus, the flow proceeds parallel to the horizontal sides, and the absence of the wall adhesion condition is sufficient to simulate the presence of an indefinitely extended fluid zone, as established by the open stream.

The boundary condition imposed at the inlet is velocity-inlet. This type of condition imposes the velocity of the flow in the specified region and adjusts the total pressure of the flow so that the imposed velocity is met. It is a condition designed specifically for incompressible flows and, therefore, appropriate for this problem. Since the total pressure of the flow is adjusted to meet the velocity, one must pay attention to the position of the inlet concerning the solid areas obstructing the flow, in this case, the cylindrical body. In fact, if the inlet is placed too close to an obstruction in the flow, the total pressure may be too non-uniform, and this worsens the quality of the results; in creating the geometry to be simulated, this problem was taken into account, and the distance of 15 diameters separating the inlet from the cylinder is sufficient for this purpose.

Within this boundary condition, it is possible to set the reference frame, which, in this case, is set as absolute. It is also possible to specify a particular velocity profile desired at the inlet; in the present study, we want to simulate an open stream, and consequently, the velocity profile at the inlet must be constant. Fluent requires you to specify how the turbulent quantities must be transported when the flow enters the fluid domain. In order to do that, several ways are available; in this study, we chose to specify the turbulent intensity and the viscosity ratio.

Turbulent intensity takes velocity fluctuations into account through an index called I, which is equal to the root mean square of the velocity fluctuation from the mean flow velocity. Typical values of this index are between 1% and 10%, and the index varies as the Reynolds number varies. For the values of the Reynolds number in this study, a turbulent intensity of 5% was considered adequate. The turbulent viscosity ratio is the ratio of Boussinesq turbulent viscosity to flow viscosity. The turbulent viscosity ratio also follows a law proportional to the Reynolds number and was set equal to 10 in this study.

The last region on which to impose a boundary condition is the outlet. The condition chosen is pressure outlet. This involves the specification of a reference system again set as absolute. It is possible to choose a desired pressure profile at the outlet; in the present study focused on the open stream, there are no constraints on the expected pressure profile, so no pressure profile has been imposed. It is necessary to set the gauge pressure at the reference outlet, which, as in the case of the inlet, has been set equal to 0 Pa.
By choosing the pressure outlet setting, Fluent requires the specification of a method to be implemented to establish the backflow direction. The backflow condition happens when, because of the fluctuations of the velocity field and the turbulence, there is a reverse flow entering the domain from the outlet. Fluent offers many possibilities for the specification of the backflow direction; in the present study, the calculation from the neighboring cell has been chosen; within this option, Fluent determines the backflow direction, computing it from the cell layer adjacent to the pressure outlet.
As in the velocity inlet, parameters must be set for turbulence simulation in the pressure outlet condition. Again, turbulent intensity and turbulent viscosity ratio are chosen to be set, the same values assigned for the velocity inlet,5 and 10, respectively, have been assigned.

With this last boundary condition set, all flow variables have been set, and the physical model is correctly set up.

Dynamic Mesh Characterisation

If the shape of the domain changes over time during the simulation, a dynamic mesh must be used in Fluent. This feature allows the mesh to be adjusted to the change in shape, either in the case where the user imposes the deformation or in the case where it results from solving the equations of motion at the current time. The latter occurrence corresponds to the present study, which is studied through the six DOF solver theory. In fact, Fluent solves the equations governing the fluid field at each instant; then, by computing the integral of the forces insisting on the cylinder, it determines the acceleration and velocity of the cylinder's centre of mass and, consequently, its position. In this way, the shape of the domain is updated, and the mesh

has to be updated, too.
There are many ways available for mesh updating. In this study, the smoothing method was used in the case of the cylinder. By implementing this method, the mesh is modified by moving the nodes of the dynamic mesh zone while preserving their number and connections. The movement is absorbed by the mesh deformation; to achieve this goal, the diffusion-based smoothing method based on boundary distance was used. It involves the choice of specific parameters that adjust the diffusion to keep the mesh quality high in the area close to the deforming edge and have most of the deformation absorbed far away in areas of less interest, where the flow is smoother, and the mesh quality remains high even in the presence of deformation.
It is also necessary to specify which mesh areas are free to deform and which are not. In this case, the square-shaped area surrounding the cylinder was chosen to be allowed to deform, while the cylinder was specified to be a rigid body. As mentioned earlier, it is necessary to specify how to calculate the motion of the rigid body. Among the opportunities offered by Fluent, there isn't the possibility of choosing a differential equation that includes damping as in equation 2.3. However, it was possible to get around this problem by using a user-defined function, which Fluent builds and implements starting from an external script specified by the user.

User-defined Function Import

As mentioned before, the UDF in this study was used to introduce damping into the equation of motion of the cylinder. Since it is defined with a script external to Fluent, it must be imported and compiled. However, it is necessary to build it first. Starting from the script, folders and system files are created, which Fluent then uses to compile the function. The journal file contains a few lines, written in bash, that perform these actions. More information regarding the contents of the UDF will be discussed later.

Reference Values Set

Reference values are used by Fluent only in post-processing; they have no function during simulation. They are used to make the results "exact," that is, to correctly calculate the derived quantities from the results actually computed during the simulation.

In the case of this study, it has been necessary to specify reference values for:

1. Area = 1m
2. Length = 1m
3. Velocity = U_∞
4. Density = ρ_s
5. Viscosity = 0.001003kg/(m s)

Solver Scheme Set

Some other parameters and algorithms need to be set before the simulation can be run.

First, a pressure velocity coupling method. As specified in the section on model definition, a segregated pressure-based algorithm was chosen for this study. For this type of algorithm, Fluent requires the specification of a method for pressure-velocity coupling. Several possibilities are available: SIMPLE, SIMPLEC, PISO, and FSM. Of these, the most recommended for transient-type simulations is PISO (Pressure-Implicit with Splitting of Operators). This algorithm is able to tolerate larger time steps and optimal under-relaxation factor for both momentum and pressure while maintaining stable computation. It is also particularly adequate in the case of RANS simulations; for all these reasons, it was considered appropriate for the present study.

It is necessary to specify which criterion Fluent should use in discretising the equations governing the motion. The second-order scheme was chosen to ensure high accuracy for both pressure discretisation and momentum discretisation.

A convergence criterion must be set; in this case, it was chosen to use the residuals. For continuity, 10^{-4} was set as the target value, while for x and y velocities, for k and ω, 10^{-5} was set. A timestep must then be set, which was chosen the same for all simulations in this study. That is, equal to one-hundredth of a convective time. Convective time is defined as the time that the undisturbed flow (traveling at U_∞ velocity) takes to travel through a characteristic length of the system, in this case, the diameter.

The simulation is initialized by hybrid initialization, through which the solver interpolates, starting from the boundary conditions, the velocity and pressure fields. It then derives from these the fields of all other quantities such as turbulence, temperature, etc. The hybrid initialization used in this study consists of 10 iterations that guarantee the solver a better starting condition in the actual resolution.

Finally, the actual resolution is launched, specifying the maximum number of iterations allowed for each time step and the total number of time steps to be simulated. Fluent will continue to iterate, remaining at the same time step, until it reaches the maximum number of iterations allowed or until it reaches the convergence criterion assigned for each simulated quantity. After that, it will update the fluid field to the next time step and proceed with the new iterations. It will terminate when the maximum number of time steps has been reached. For this study, the maximum number of sub-iterations was set to 20, which is appropriate for the convergence criteria chosen and the convergence speed of the simulations. The number of time steps was different for each simulation.

Report Definition

In this section of the journal file, commands needed to store the simulated variables values have to be written. In this case, the values of both the lift and drag coefficients were saved. In addition, the motion history of the mass centre of the cylindrical body was stored. All of these variables are needed for the post-processing of the simulations, but they're also required to check the convergence of the simulations. In fact, by observing the history of motion, we can check if the simulation has reached a regime or is still in the transitory phase; the drag and lift coefficients can be helpful in the same way.

2.2.2 User-defined function

A user-defined function is a function that can be used to enhance the possibilities of Fluent, such as creating boundary conditions, materials with specific properties, customized model parameters, etc. They consist of a source file written in the C programming language, which is then compiled or interpreted by Fluent. A compiled UDF was used in this study; Fluent takes two separate steps to use it: first, it builds the UDF library and then implements its contents. In the course of this study, it was necessary to create a UDF to include the damping of the mechanical system among the parameters that govern the motion of the cylindrical body since, in Fluent, it was possible to create only elastic models.

The structure of the UDF can be divided into four parts.

The first requires that, using the command "`#include`", libraries are imported. In particular, "`#include "udf.h"`" allows the use of "`DEFINE`" macros for the definition, in this case, of parameters and degrees of freedom. "`#include "dynamesh_tools.h"`" allows access to the time macros of the dynamic mesh. Finally, "`#include "math.h"`" provides access to the standard C library that contains definitions of functions and types used for mathematical operations.

In the second section, the variables of the function are declared; in this case, it was necessary to declare: the position of the centre of mass of the cylinder and its velocity, the mass of the cylinder, the elasticity of the mechanical system and its damping. Regarding mass stiffness and damping, the values are constant and user-defined for each simulation, while the position and velocity of the cylinder's center of mass are calculated by Fluent.

In the third section of the UDF, the degrees of freedom of the mechanical system are defined. In this case, the system has only one degree of freedom. It is free to translate vertically (along the y axis), translations along x and z are blocked, as are the three rotations along each axis. In addition, the value of the previously stated mass is assigned to the cylinder. In the fourth section, the previously declared variables, the position and velocity of the centre of mass are defined so that Fluent updates their values over time. Finally, there is the differential equation of motion into which all variables are entered. Note that Fluent already counts inertia forces, so only the terms related to damping and stiffness appear explicitly.

2.3 Variable Selection

When approaching the choice of values to be assigned to the variables governing the system, one notices that there are many variables and that many equations link them together. In fact, only a few variables can be chosen completely independently. This choice is critical because, by imposing some variables to the exclusion of others, it influences the areas in which the system's behaviour can be observed.
In order to make this choice, it is therefore appropriate to comment on the purpose of the analysis and the fields of applicability of these configurations. The first observation that can be made is to consider the fact that the purpose of the system is to extract as much energy as possible from the flow, and therefore, it would be appropriate to calibrate the system's parameters so that this happens.
Another thing to consider is the physical feasibility of the system whose behaviour is simulated. In the realisation of a mechanical system, in fact, some parameters can hardly be variable; just think of the mass of the cylinder or the stiffness of the springs that control its movement; to make these parameters vary, one has to complicate the mechanical system, and this is not appropriate in a phase of the study in which one only wants to explore the behaviour of the model as the damping varies.

Regarding the first observation, the maximum energy transfer, between fluid and oscillating body, occurs when the lock-in condition takes place, as stated by De Vanna et al. (2023) de Vanna and by Badhurshah et al. (2019). We need to consider the conditions under which the mechanical system exhibits suitable characteristics with respect to the flow so that the lock-in state can be achieved. This condition, in the case of no damping, only occurs when the system's fundamental frequency corresponds to the vortex detachment frequency. The Strouhal number can explain this condition well.
Two Strouhal numbers must be used to characterize the system, one associated with the body motion:

$$St_y = \frac{f_y D}{U_\infty} \tag{2.13}$$

and one associated with the flow:

$$St_v = \frac{f_v D}{U_\infty} \tag{2.14}$$

where f_y indicates the fundamental frequency of the mechanical system in the absence of damping $\mu = 0$, i.e., in the dimensionless case :

$$\rho A\ddot{y}/D^2 + \xi y = 2cy \tag{2.15}$$

while $f_v$indicates the frequency associated with vortex shedding.

To better describe this situation, it is appropriate to introduce the reduced speed thus defined:

$$Ur = \frac{U_\infty}{f_n D} \tag{2.16}$$

where f_n is the natural frequency of the cylinder:

$$f_n = \frac{1}{2\pi}\sqrt{\frac{k}{m}} \tag{2.17}$$

The lock-in state is obtained when:

$$St_y = \frac{1}{Ur} \tag{2.18}$$

and it is appropriate to choose which parameters, among those governing the motion, to impose in order to achieve this condition.

First of all, remember that we want to maintain a non-dimensional approach to the problem and, therefore, the geometric parameters remain normalised, $D = 1m$. Also, some of the parameters concerning the fluid can not be chosen, e.g. the density value ρ_∞, since the operating fluid adopted is water.
Next, we can consider the fact that we want to observe how the system is affected by damping as the flow velocity varies with different values for each simulation. To vary these values, we chose to impose different values of U_r and, from these, derive the values of U_{infty}. The ranges of velocity to be simulated were evaluated to focus on the most promising values for each case, in order to best represent the lock in area.
Another parameter to be imposed is, obviously, the mechanical damping of the system c. The choice of values for this parameter must remain unconstrained so that different values can be imposed for each group of simulations; the choice of these values was evaluated on a case-by-case basis.
In order to have a reference concerning the intensity of the imposed damping, various values of the damping ratio were imposed, starting with the free case and proceeding with gradually increasing damping intensities so that we could accurately observe the effect of this parameter in the interaction

between fluid and mechanical system.
The damping ratio ζ is defined as follows:

$$\zeta = \frac{c}{c_{\mathrm{cr}}} \qquad 2.19$$

where c_{cr} is the critical damping of the mechanical system, which is an excellent benchmark since it represents the smallest damping value for which there are no free oscillations, and it is defined as follows:

$$c_{\mathrm{cr}} = 2\sqrt{km} \qquad 2.20$$

After these considerations, when analysing the remaining parameters, we realise that it is still possible to assign values to at most two parameters independently.

In this study, we chose to keep constant, for each set of simulations, the value of the first natural frequency of the free system defined by the formula 2.17. This choice implies a series of constraints between the other variables; in fact, observing the equation 2.17, it can be seen that by imposing a value for the first natural frequency of the system, the values of stiffness and mass of the body can no longer both be chosen independently.

The second parameter on which a constant value was imposed for all simulations is the non-dimensional stiffness ξ.
This choice was made because preliminary simulations yielded promising results about the lock-in condition, which always seems to be satisfied in the cylindrical case with zero damping, as the undisturbed velocity varies.
With the imposition of a value for xi the problem is entirely mathematically defined; in fact, recalling the definition of xi (equation 2.9), the following steps can be performed by substituting the undisturbed flow velocity U_∞, obtained from equation 2.16:

$$\xi = \frac{k}{\rho_\infty U_\infty^2} = \frac{k}{\rho_\infty U_r^2 D^2 f_n^2} \qquad 2.21$$

now f_n, defined in equation 2.17, can be substituted into the previous equation giving:

$$\xi = \frac{1}{\rho_\infty U_r^2 \frac{1}{4\pi^2}\frac{D^2}{m}} \qquad 2.22$$

where k was simplified from the fraction.

In order to obtain a relationship between xi and rho, one can proceed by substituting in 2.22 the definition of the mass, which, for the cylindrical case, is:

$$m = \frac{\rho_s \pi D^2}{4} \tag{2.23}$$

Note that this is a mass per unit length, consistent with the two-dimensional model used for the study.

The following relation is obtained:

$$\xi = \left(\frac{\rho_\infty}{\rho_s} \frac{U_r^2}{\pi^3} \right)^{-1} = \frac{\rho \pi^3}{U_r^2} \tag{2.24}$$

where ρ is the ratio of cylinder density to water density defined in the equation 2.7. From the relation 2.24, since π is a constant, it can be seen that by imposing a constant value for ξ, the ratio between the square of U_r and ρ must remain constant.
Since the relative flow velocity U_r, the natural frequency f_n and the diameter D are imposed, the undisturbed flow velocity U_∞ is uniquely determined. Similarly, since xi is imposed, the values of the density ratio are derived from the 2.24. Then, from the density ratio, we derive the density of the solid ρ_s given that of the fluid ρ_∞. Finally, given the geometry, the mass of the cylinder is derived.
It is now sufficient to derive the stiffness k to characterise the system. Explicit from the equation 2.21, the value of the stiffness k can be obtained:

$$k = \rho_\infty U_r^2 D^2 f_n^2 \xi \tag{2.25}$$

For this first macro group of simulations, which will later be called “constant ξ simulations”, the system’s operating conditions are entirely defined, and it is possible to proceed with the dynamic simulations.

Further considerations can be made concerning the system at constant ξ. From the equation 2.25, it can easily be observed that k is directly proportional to U_r^2. Since U_r is made to vary in each group of simulations, k assumes a wide range of values. From the point of view of the physical realisation of the mechanical device, this is not optimal, as one would have to vary the stiffness of the springs a lot when the undisturbed flow velocity varies.

To overcome this problem, an additional parameter called k^* was introduced into the system. It is a modified stiffness defined as follows:

$$k^* = \frac{k}{k_0} \tag{2.26}$$

where k_0 is the stiffness of a spring which, subjected to a compression equal to the length one diameter of the cylinder, produces a force equal to the weight of the cylinder itself (where the gravitational acceleration is set equal to $g = 9.80665\,\mathrm{m/s^2}$):

$$k_0 = \frac{mg}{D} \tag{2.27}$$

The link between k^* and the dimensionless stiffness of the system ξ is as follows:

$$\xi = k^* \frac{mg}{\rho_\infty {U_\infty}^2 D} \tag{2.28}$$

From the formulas 2.26 and it can be seen that assigning a constant value to k^* has two effects:

1. It implies the constancy of k.
2. It allows ρ and U_r to be chosen independently.

Thus, as in the constant-ξ case, the geometric parameters D, the fluid density ρ_∞, the damping ratio ζ and the relative velocity U_r assume imposed values. In addition, a constant value is imposed on k^* which also implies a constant value for k. A constant value is also imposed for the density ratio ρ.
The constancy of the values of k and rho as the flow velocity varies, unlike in the constant ξ case, allows the practical realisation of the system while continuing to refer to dimensionless quantities; this would not have been possible without the introduction of the parameter k^*.

The values for the remaining parameters can be determined as follows: the undisturbed flow velocity U_∞ comes from equation 2.16 given f_n and D, the density of the body ρ_s is determined can be computed via the product between ρ and ρ_∞ which are both assigned values, the mass values is than calculated multiplying the solid density for the volume remembering that the model is bi-dimensional and therefore the mass is a mass per unit length. Than the dimensional stiffness k is calculated from equation 2.26 after the determination of k_0 value, while the non-dimensional stiffness, ξ, values come from equation 2.3. Finally the parameters concerning the damping are determined in the same way as the ξ-constant case that is the imposition of a constant damping ratio ζ for each set of simulations and the real damping comes from equation 2.19. With these explanations, even for this second type of equation, the mathematical problem is entirely formulated.

To summarise, for each configuration of the system analysed, i.e. cylinder in cross-flow configuration or square-base prism in cross-flow configuration, two sets of simulations were run:

1. ξ-constant simulations
2. k^*-constant simulations

For both of these cases, the system's behaviour under varying imposed damping values and varied U_r imposed values was analysed.

Having set up the journal file and the source file for the UDF, the problem has been numerically set up. With the characterisation of mathematical parameters, the problem is entirely set up and, therefore, simulations can be launched.

- III -

Cylinder

This chapter is dedicated to the open stream configuration with the cylinder as the oscillating body. The first section contains a description of the computational grid used for the simulations and important information regarding the quality of the mesh. Next, some information is presented regarding the convergence of the simulations and strategies to decrease the convergence time of the simulations. Finally, the results in frequency analysis, displacements and powers are presented and discussed, illustrating the ξ-constant and k^*-constant cases separately.

3.1 Cylinder mesh

The mesh used in the current study has been extensively tested in a sensitivity study comparing it with other meshes of different refinement. Its behaviour as a function of the turbulence model adopted was also studied.

The chosen mesh has about 40K elements and represents a good compromise between the more refined 90K elements mesh and the coarser 20K elements mesh, both in terms of computational performance and accuracy.

In addition to the sensitivity test, the mesh was also validated by comparing the results obtained with experimental data in literature, in particular with the results obtained by Achenbach and Heinecke (1981) This comparison confirmed the good performance of the mesh and provided useful information for the selection of the best turbulence model.

Three different turbulence models were tested. A one-equation model (Spalat-Allmaras), developed by Spalart and Allmaras (1994), is the least

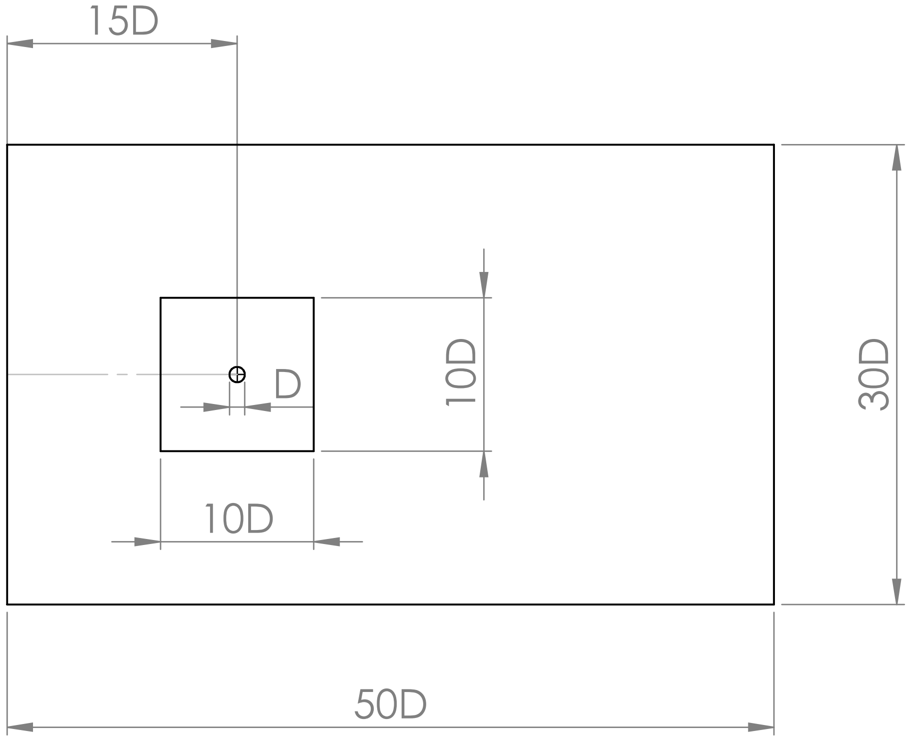

Figure 3.1: *Domain geometry with parametric dimensions in function of the diameter*

computationally expensive and can generally perform well for applications involving wall-bounded flows. A two-equation model (k-ω Shear Stress Transport) developed by Menter (1994), which generally performs very well thanks to the combination between the k-ω and k-ϵ model, which are exploited for their best behaviour in different zones of the fluid domain (wall zone or free-stream zone), since it implements two equations it has a higher computational cost than the previous one. A four equation model (Transition Shear Stress Transport) developed by Menter et al. (2006), it implements equations for "γ" and "*Retheta*" in addition to the "k" and "ω" equations of SST, it has the highest computational cost of the three simulated models. The chosen turbulence model is k-ω Shear Stress Transport, since among the models adopted (k-ω Shear Stress Transport, Transition Shear Stress Transport and Spalart-Allmaras) it gives the best results in both steady and unsteady simulations.

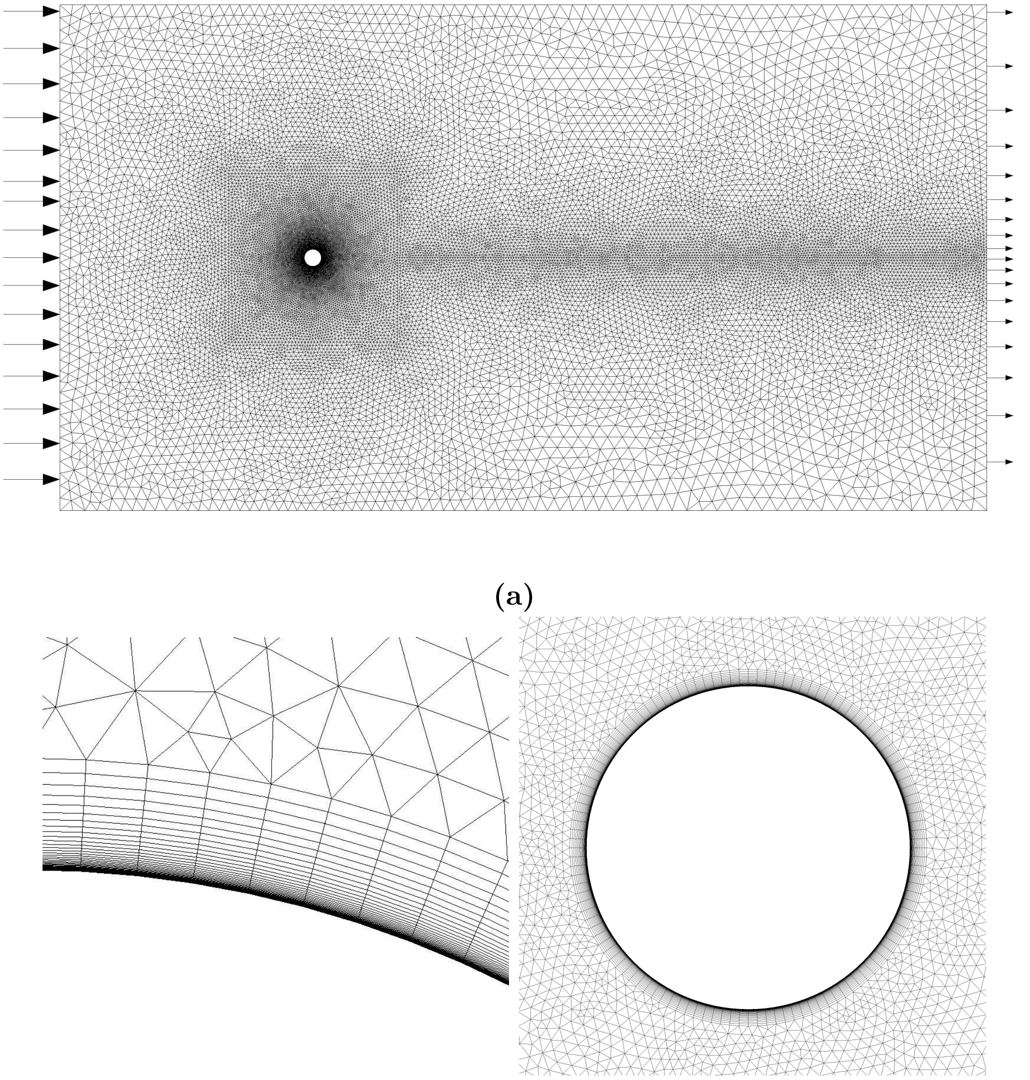

(a)

(b) **(c)**

Figure 3.2: *Full fluid domain (**a**); cylinder wall zone (**b**); focus on the cylinder (**c**).*

This section briefly introduces the geometry of the mesh. The simulated fluid domain is shown in figure 3.1. In order to maintain the generality of the problem, the domain was designed using the cylinder diameter as a parameter; it is 50 diameters wide and 30 diameters high. The cylinder is located 15 diameters from the inlet, and it is surrounded by a square zone with a side of 10 diameters, which is still part of the fluid zone; this is the dynamic mesh zone that has been assigned to allow the adaptation of the grid to the movements of the cylinder.

A hybrid mesh, composed of triangular and quadrangular elements, has been used. It is unstructured everywhere except for some square cell layers (inflation layers) around the cylinder, which form a so-called "O-grid". This approach allows the behaviour of the boundary layer to be correctly captured; in this respect, the y^+ parameter has also been evaluated, and the values it assumes are less than one with a good margin along the entire cylinder wall area; this detail can be seen in figure 3.2b.

At the same time, the use of a hybrid mesh allows for excellent filling of the fluid domain while maintaining good skewness and orthogonality parameters.

Finally, in order to accurately capture the behaviour of the fluid in the areas of interest, the cell density was increased both in the area surrounding the cylinder and in the wake area along the entire length of the domain, as can be seen in figure 3.2a. Clearly, these are the areas of most significant interest, for it is in these that the pressure and velocity fields are most altered by vortex formation, which must be properly captured.

3.2 CONVERGENCE OF SIMULATIONS

A convergence criterion was discussed in the setup of the simulations, the imposition of a target value for the residuals set equal to 10^-5. However, once this value is reached, the simulation does not terminate because the solver proceeds by updating the momentum field at the next timestep; the updated pressure and velocity fields produce a new thrust on the cylindrical body, and the simulation enters a loop where the residuals never consistently fall below the threshold value. If only this convergence criterion had been imposed, the simulation would never have ended. In fact, the cylinder would continue to oscillate indefinitely since the undisturbed flow velocity always remains nonzero. Therefore, it is necessary to impose an additional criterion to establish the end of the simulation.

In this study, for each simulation, the maximum number of timesteps that could be simulated by Fluent was imposed, and in order to verify the actual convergence of the simulations, it was necessary to refer to the displacements of the body over time. Typical cylinder behaviour involves an initial transient part during which the amplitude of the oscillations varies until a specific amplitude, generally different for each case, is reached and then maintained. Convergence was considered to have been reached when the variation in oscillation amplitude ceased. In addition, after convergence was reached, some margin was maintained, which was necessary to accurately compute time-averaged values of displacements and power and have adequate data for good frequency analysis.

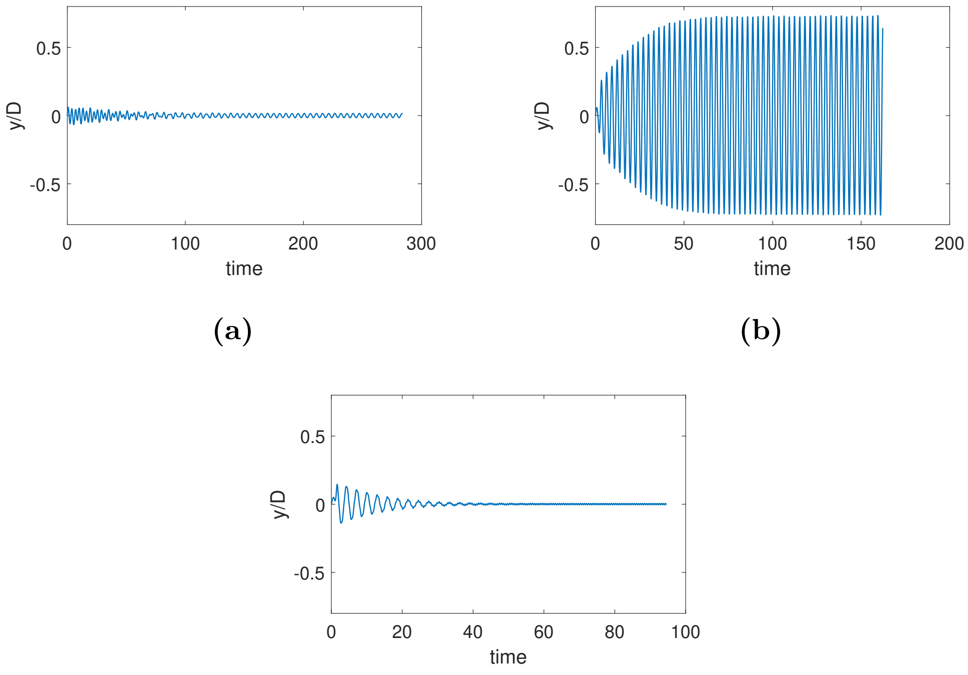

(a) **(b)**

(c)

Figure 3.3: *Typical displacements of the cylinder's centre of mass over time. Note that the x-axis shows dimensionless time values. The graphs shown refer to the case with the circular cross-section for simulations conducted at* $k^* = 0.5$ *and* $\zeta = 0.01$*. In particular, (a) refers to* $U_r = 2.0$*; (b) refers to* $U_r = 7.0$*; and (c) to* $U_r = 15.0$*.*

The simulations conducted take a long time to converge. In addition, they consume many hours of computing time due to their large number, and the hours available were limited. Therefore, techniques were adopted to try to reduce the time required for convergence. In particular, the choice was made to impose a non-zero initial velocity on the cylinder, with different values for each simulation, attempting to guess the amplitude at the convergence of the oscillations. The choice of initial velocities was based on the available data, giving higher velocities for areas where the lock-in condition was expected.

Figure 3.3 shows the displacements, normalised to the diameter, for 3 different velocity values U_{infty} from the same set of simulations. In these figures, one can easily identify the zones of transient regime and the zones for which convergence has been achieved. One can also note the significant difference in displacement between 3.3b with respect to 3.3a and 3.3c cases. The three velocity values have, in fact, been purposely chosen to highlight the difference in the behaviour of the cylindrical body when outside the lock-in zone (figures 3.3a and 3.3c) and when inside (figure 3.3b).

3.3 Dynamic analysis

The simulations were divided into two main groups, one with all cases at constant ξ and one with all cases at constant k^*. The data were post-processed by a frequency study of the cylinder displacements and the power produced as the damping changes. The results give important information on the effect of mechanical damping on the system and the conditions required to operate the device properly.

The figure 3.4 (from De Vanna et al. (2023)) gives an excellent graphical description of the lock-in condition; one can, in fact, see the relative movement between the cylindrical body and the primary vortex downstream of it, which is responsible for the lift force that moves the cylinder. It can be seen that the vortex is in a very close position to the cylinder in the 3.4b and 3.4d figures, while in a more distant position in the 3.4a and 3.4c figures, the first two figures correspond to conditions of maximum displacement while the second two to conditions of maximum velocity of the cylindrical body. In fact, according to Guilmineau and Queutey (2002), when the oscillation frequency of the cylinder and the detachment frequency of the vortices have similar values (Guilmineau suggests frequency ratios between 0.8 and 1.20), the primary vortex downstream of the cylinder assumes the following behaviour: it tends to approach the cylinder when the amplitude is maximum, and then suddenly switches to the other side of the cylinder, changing the pressure field, and exerting a force on the cylinder that tends to make it accelerate in the opposite direction.

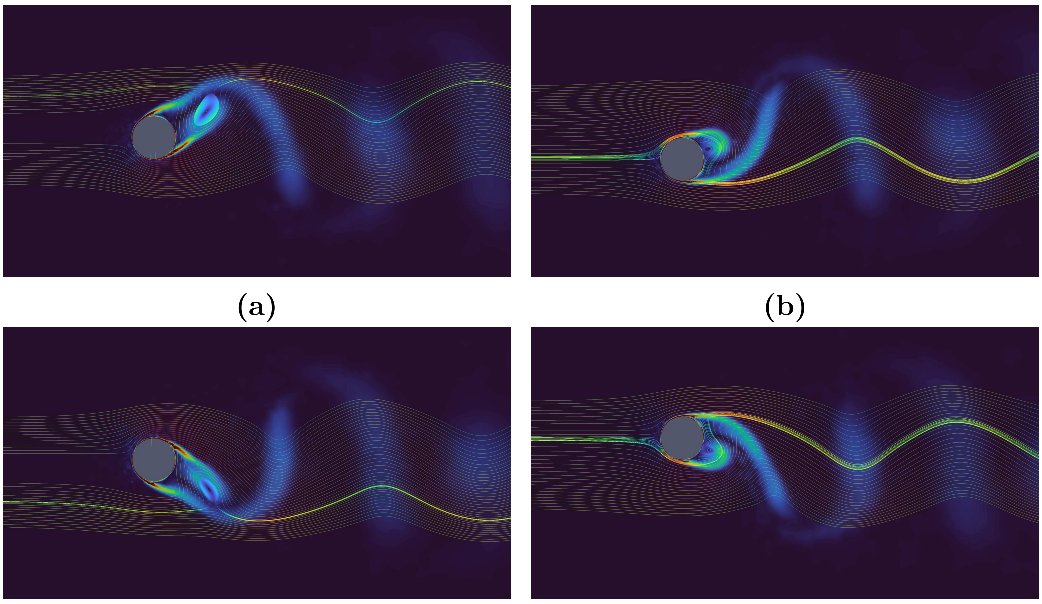

(a) **(b)**

(c) **(d)**

Figure 3.4: *Velocity field streamlines and ω_z vorticity contours for an oscillating cylindrical body.*

3.3.1 CONSTANT ξ CASES

In this paragraph, we present the results of simulations conducted a constant ξ. Note that, as specified in paragraph 2.3 , this case is of purely theoretical interest since the imposition of constant values on the natural frequency of the system f_n and the non-dimensional stiffness ξ impose constancy on the ratio U_r^2 to ρ. Therefore, since U_r varies for each simulation, ρ assumes on very different values in the simulations, as is the case for the stiffness k. However, it was chosen to explore this configuration because, from preliminary simulations, it was seen that, in the case of no mechanical damping, the constancy of ξ causes the lock-in condition to be maintained for all velocities, and it was desired to study the effect of damping with respect to this condition.

The values imposed on the variables for this set of simulations are as follows:

- $\xi = 9$
- $f_n = 0.1$
- $\zeta = 0.00,\ 0.01,\ 0.05,\ 0.1$
- $U_r = 1.5 - 20.0$

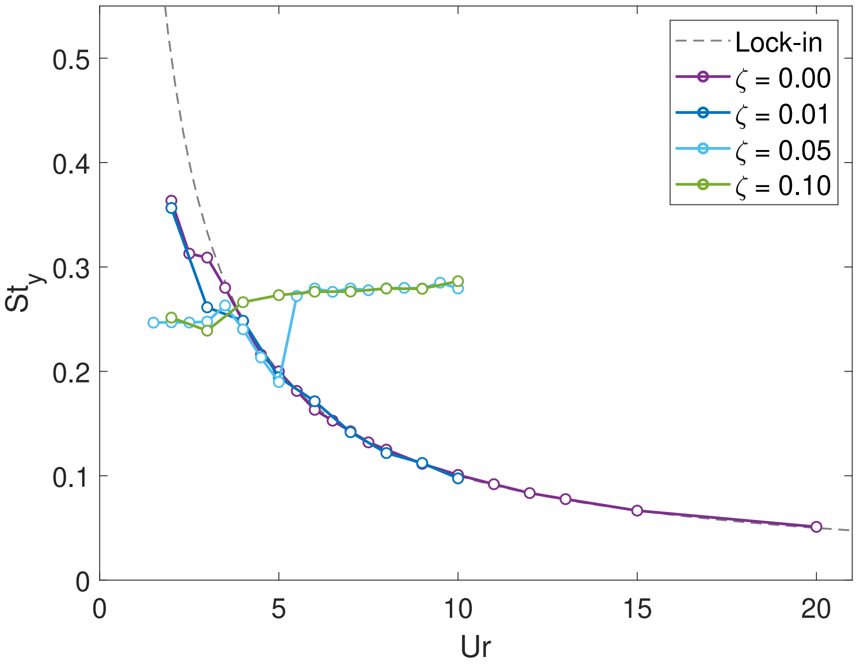

Figure 3.5: *The plot of the Strouhal number* St_y *versus velocity* $Ur = U_\infty/f_nD$ *for simulations at* $\xi = 9$ *and values of the damping ratio given in the legend.*

As far as the frequency analysis is concerned, the Strouhal number plot against the non-dimensional velocity is plotted; in addition to the simulation results, the curve $1/U_r$ is also plotted, which represents the matching condition between the vortex shedding frequency and the natural frequency of the system. That is, the points that belong to that curve represent conditions for which the system is in a lock-in condition. It can clearly be seen that the points that make up the curve in purple, at zero damping, $\zeta = 0$, all belong to the curve dashed in grey. This indicates that the lock-in condition has been maintained at zero damping for any simulated velocity.

Turning our attention to the other curves instead, we can clearly see that the damping dramatically affects the speed range for the lock-in condition. In fact, for $\zeta = 0.05$, the lock-in condition is maintained for only U_r values between 3.5 and 5; while increasing the value of the damping ratio even further, the cylinder is practically never in lock-in.
It should also be noted that, outside the lock-in zone, the value of the Strouhal number St_y is consistently around 2.7; this value does not differ from what is suggested by Kaneko et al. (2008). However, the Reynolds values Re_∞, typical of these simulations, are slightly higher than those for which Kaneko suggests the constancy of the Strouhal number with respect to Reynolds. They, in fact, reach up to $7 \cdot 10^6$; despite this, it is shown that the system remains in lock-in condition throughout the simulated velocity range for both the free case and the case with $\zeta = 0.01$.

The root mean square value of the displacements was studied for analysis of the cylinder oscillation amplitude, it can be seen in figure 3.6. Interesting results were obtained. About the zero-damping curve, as expected, the displacements are more significant than in all the other curves; the bell horizontal amplitude is also greater than in the cases with non-zero damping. This agrees with the graph 3.5, in which the purple curve corresponds to a broader range of lock-in velocities. It can also be seen that, although the lock-in condition is maintained for high values of U_r, the displacements tend to become smaller and smaller.
As for the curves with damping ratio values other than zero, these show the same effects as those observed in graph 3.5. Damping, as already observed, has, in fact, intense effects on the range of velocities at which the lock-in condition is maintained, and in addition to this, it also has an important effect in lowering the peak amplitude of the oscillations; already for $\zeta = 0.01$ we obtain a reduction of about 25% of the maximum peak of y_{rms}.

Finally, it should be noted that in addition to the curves for the simulations performed, an exponential curve interpolating the peaks was also plotted, which shows that as the damping increases, the maximum displacement values are obtained for lower reduced velocities.
Since this study aims to derive guidelines for energy production using energy harvesters, it is interesting to observe the power values produced in the various simulations, even though the constant-ξ case is a case of primarily

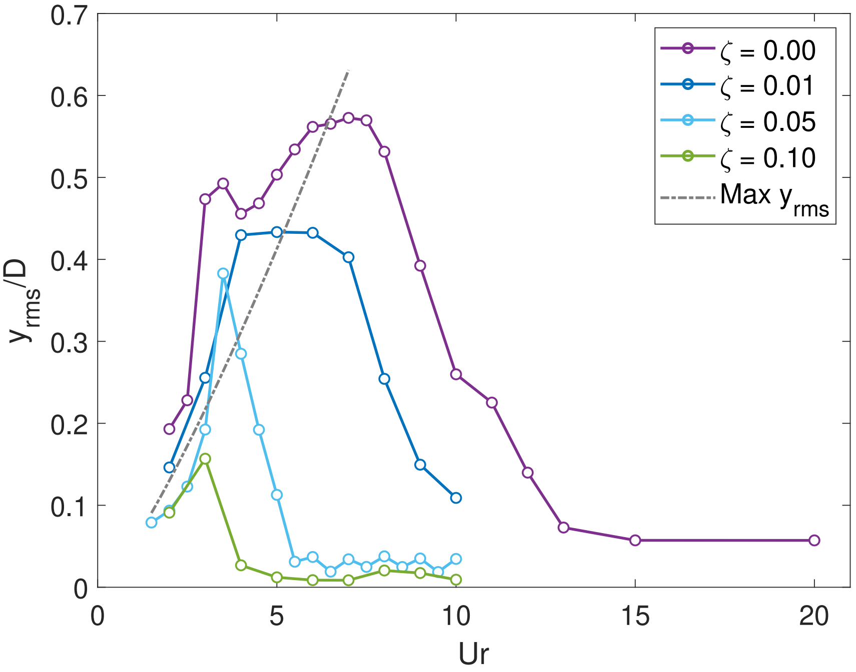

Figure 3.6: *The plot of the* y_{rms}/D *versus velocity* $Ur = U_\infty/f_nD$ *for simulations at* $\xi = 9$ *and values of the damping ratio given in the legend.*

theoretical interest.

In this study, we were only interested in the values of mechanical power rather than those of electrical power, which will be easy to obtain once an energy conversion device, piezoelectric or electromagnetic, has been chosen. From the instantaneous velocity values of the cylinder's centre of mass, it is easy to calculate the mechanical power at each instant. To maintain the study's dimensionless approach, a non-dimensional power parameter, the P^*, has also been defined in this field:

$$P^*(t) = \frac{\dot{y}(t)}{U_\infty} \frac{F_y}{1/2\rho_\infty D U_\infty^2} \tag{3.1}$$

The results represented in the graph 3.1 reflect what has already been shown in the case of displacements. However, there are some differences; it can be seen that all the curves, including the one with zero damping, are characterised by a great peak between $U_r = 3$ and $U_r = 4$; the maximum height of the peak decreases as ζ increases, and the range of velocities for

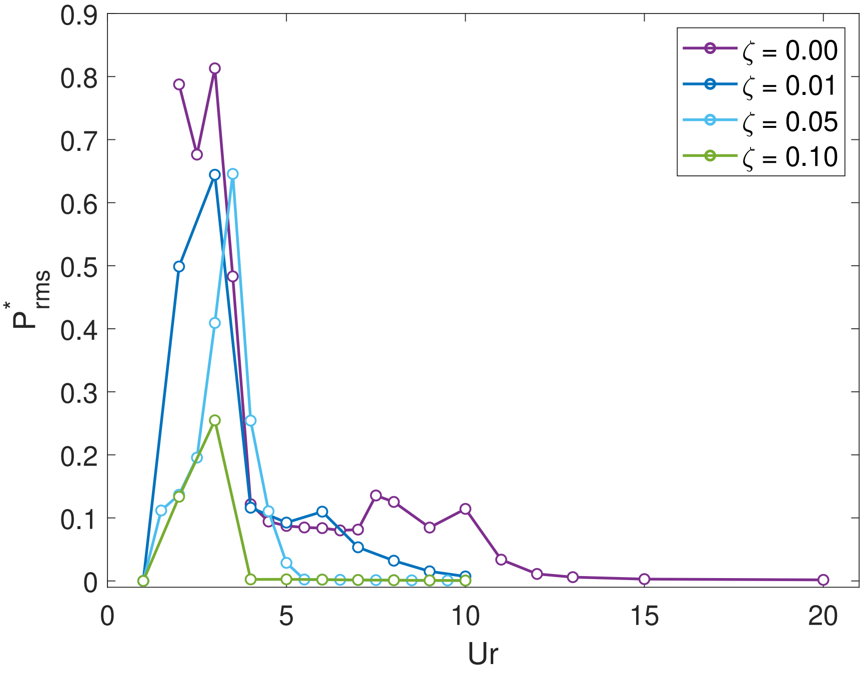

Figure 3.7: *The plot of the* P^*_{rms} *versus velocity* $Ur = U_\infty/f_nD$ *for simulations at* $\xi = 9$ *and values of the damping ratio given in the legend.*

which a significant amount of power is produced decreases, but less intensely than observed for the displacements.

3.3.2 Constant k^* cases

This section reports the results of simulations performed at constant k^* values. This case, compared to the previous one, is of greater practical interest since the parameter k^* (formula 2.26) has been purposely defined so that the values of ρ and k remain constant, while k^* also remains constant. The simulations performed for this case aim to highlight the effects of the damping ratio ζ on the system over a certain speed range.

The values imposed on the variables for this set of simulations are as follows:

- $k^* = 0.5$
- $\rho = 5$
- $\zeta = 0.001, 0.005, 0.010$
- $U_r = 2.0 - 20.0$

The value $k^* = 0.5$ was specially chosen and, according to the 2.26 definition, corresponds to half the weight force of the body when the spring is compressed by one unit of length.

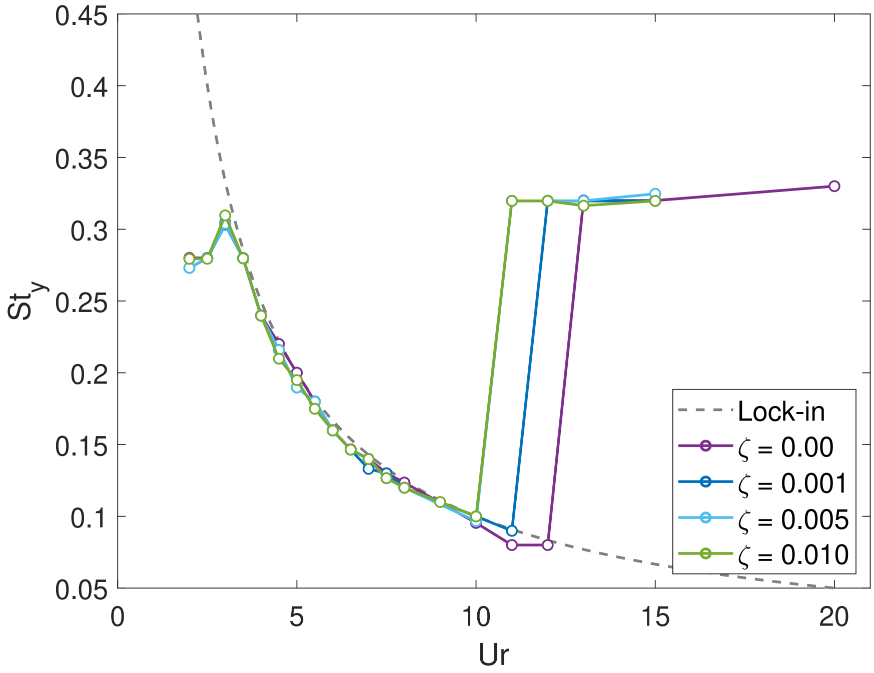

Figure 3.8: *The plot of the Strouhal number St_y versus velocity $Ur = U_\infty / f_n D$ for simulations at $k^* = 0.5$ and values of the damping ratio given in the legend.*

Starting from the frequency analysis, Figure 3.8 shows the Strouhal number versus relative velocity. It can clearly be seen that all the curves have very similar behaviour, presenting an initial zone, for $U_r < 3$ where the lock-in condition does not exist; in fact, the Stourhal number appears to have a constant value of approximately 0.28. For the speed range between $U_r = 3$

and $U_r = 10$, the lock-in condition is guaranteed for all the curves, and this can be seen by the fact that they correspond to the grey dashed line, whereas, for higher speeds, the behaviour differs. In fact, as the damping ratio increases, the range of velocities for which the lock-in condition exists decreases slightly. For relative velocities higher than $U_r = 12$, all four curves assume the same behaviour again.
One can note the fact that outside the lock-in range, the Stourhal number again assumes a constant value as hypothesised; one can also note that, even though for these simulations, the typical Reynolds values oscillate between $3 \cdot 10^4$ $3 \cdot 10^5$, St_y assumes values of approximately 0.32, higher than those suggested by Kaneko et al. (2008). The damping ratio seems to have little effect on the system, with a slight reduction in the lock-in range being the only appreciable one. Compared to the previous case, ξ constant, damping seems a much less relevant parameter.

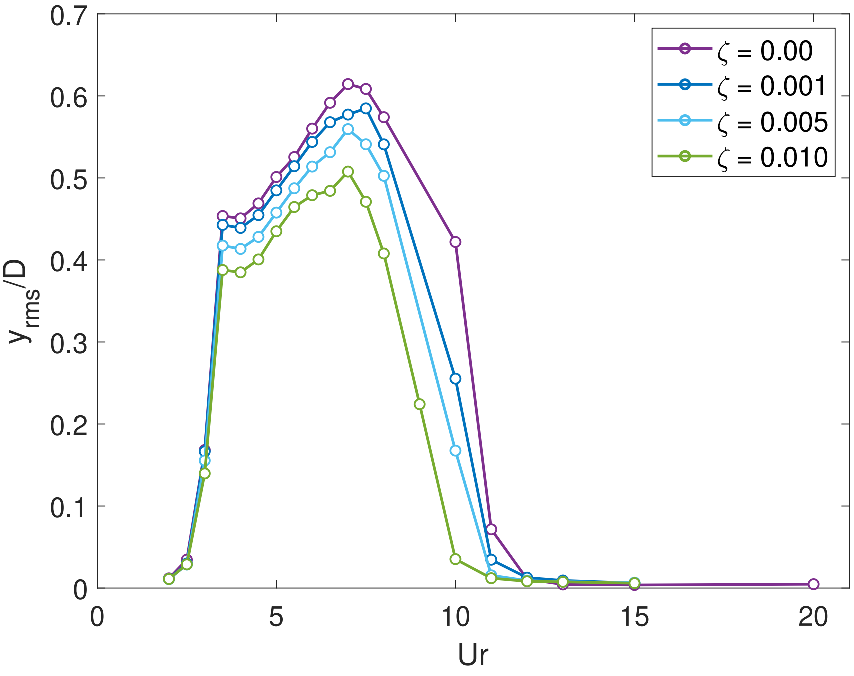

Figure 3.9: *The plot of the y_{rms}/D versus velocity $Ur = U_\infty/f_nD$ for simulations at $k^* = 0.5$ and values of the damping ratio given in the legend.*

Also in this case at constant k^*, the amplitude of the oscillations was analysed as the velocity varied. The graph 3.9S represents the results obtained. The curves represented are all very similar, and this is precisely the behaviour expected of a spring-dumping-mass lumped model. In fact, As the damping ratio ζ increases, the oscillation amplitude decreases for any velocity. The curves are all very similar: they show significant displacements starting from $U_r = 4$ and the oscillation amplitudes continue to increase up to $U_r = 7.5$ and then decrease quite rapidly. Another effect of the damping is also observed, as already shown by the graph 3.8, the amplitude of the lock-in zone decreases slightly at its right edge. Even in this analysis of the amplitude of the oscillation, a clearly different effect of the mechanical damping on the system can be seen compared to the effect in the constant ξ case.

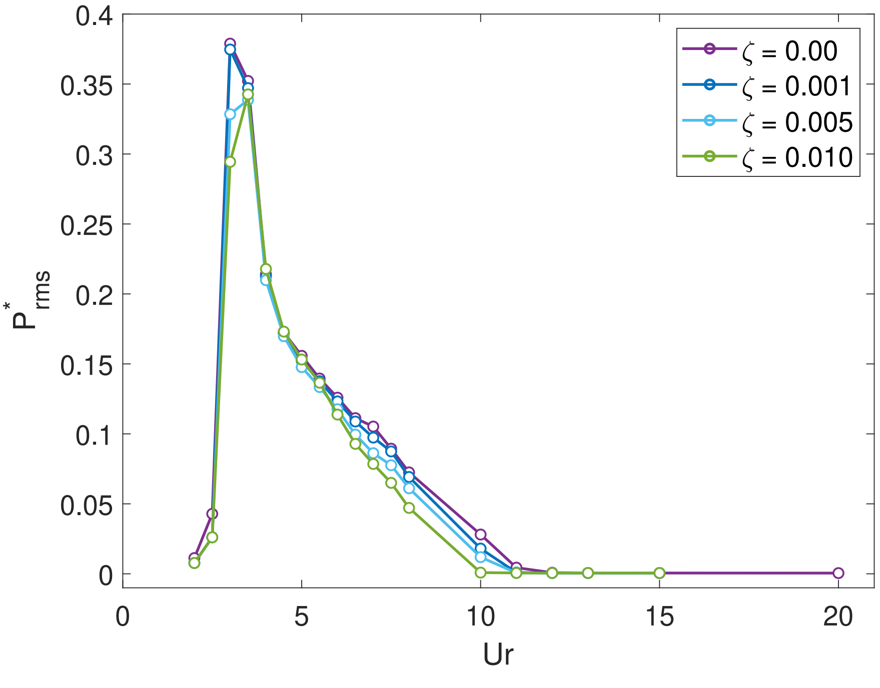

Figure 3.10: *The plot of the* P^*_{rms} *versus velocity* $Ur = U_\infty/f_nD$ *for simulations at* $k^* = 0.5$ *and values of the damping ratio given in the legend.*

For the analysis of non-dimensional power, roughly the same conclusions can be drawn as for the study of amplitudes. The graph 3.10 shows a very high peak for velocity values of $U_r = 3$, which is formed abruptly; increasing

the relative velocity further, the power produced decreases almost linearly to become practically null for values of $U_r = 10$ or greater. The damping ratio also has little effect on the power produced; the curves are, in fact, all almost overlapping; it can only be seen that as ζ increases, the power values decrease slightly for each velocity value.
The graph 3.10 gives good information for the design of an energy harvester; in fact, it clearly identifies the speed range at which this mechanical system performs well and also shows that the system well tolerates the presence of damping.

In conclusion, it can be said that the system configuration adopted for this case at constant k^* seems to be promising for an energy harvester. In fact, the mechanical system, in order to produce electrical energy, will certainly be coupled with an energy conversion device, and a certain mechanical damping will surely characterise the latter. The analysis carried out in this study shows that the mechanical system tolerates the presence of damping very well; furthermore, the fact that the range of speeds at which large oscillations are obtained is limited at the top protects against possible malfunctions due to excessive flow velocities. Should the fluid velocity increase excessively, the cylindrical body will cease to oscillate once it exits the lock-in range.

- IV -

SQUARE-BASED PRISM

This chapter is focused on the open stream configuration with a square-cross section. This type of section was chosen because, from preliminary studies, it seemed to be promising from the point of view of the maximum amplitude of oscillation and the range of velocities at which it takes place. Compared with the case with the circular cross-section, in fact, larger U_r values predict larger amplitudes of oscillation; thus, the configuration with the square could be exploited where flow velocities were too high for the configuration with the cylinder.
Below, the setup differences from the configuration with the cylinder will be exposed, followed by the mesh presentation. Finally, simulation results will be exhibited with a similar structure as in the previous chapter.

4.1 SETUP DIFFERENCES

The setup adopted for this configuration was kept as similar as possible to that used for the cylindrical configuration. However, there are some differences, both in the mechanical model and in the computational setup.

The mechanical model is basically the same as the one presented in Chapter 2; the differential equation of motion remains the same, but now the side, L, is used instead of the diameter D. The non-dimensional quantities then become:

$$y = \tilde{y}/L \qquad 4.1 \qquad\qquad t = \tilde{t}U_\infty/L \qquad 4.2$$

and consequently the non-dimensional equation of motion becomes:

$$\rho A\ddot{y}/L^2 + \mu\dot{y} + \xi y = 2cy \qquad 4.3$$

where the non-dimensional damping is:

$$\mu = c/(\rho_\infty U_\infty L) \qquad 4.4$$

and the lift coefficient is:

$$c_y = F_y/q_\infty \qquad 4.5 \qquad\qquad q_\infty = 1/(2\rho_\infty U_\infty^2 L) \qquad 4.6$$

The remaining parameters remain unchanged.

Regarding the computational setup, there are differences in the solving method used in Fluent. About the definition of the solver model, pressure-based is still used because it is the most suitable in this case as well. In fact, the configuration is practically unchanged from the cylinder case; the simulations conducted are transient, the fluid used is incompressible, and the imposed boundary conditions are the same. However, it was not possible to use the PISO algorithm for pressure-velocity coupling. In fact, by trying to use this method, the simulations were being stopped by Fluent after a few iterations due to the collapse of some cells. This probably happened because the square underwent too large displacements within a timestep, and therefore, Fluent could not tolerate them. It was desired to maintain the same proportion between the chosen timestep and the convective time for each simulation so as not to overly lengthen the convergence time, which, already with the previous setup, was very long. Therefore, the coupled method was used as the pressure-velocity coupling algorithm. This method, in fact, offers some advantages over the segregated approach; it is more robust when compared with SIMPLE or PISO and is, in addition, able to tolerate larger timesteps. Generally, it performs well even with coarser meshes, and this serves the purpose. The main difference from the PISO algorithm is that the momentum and continuity equation, based on pressure, are solved together instead of separately. This makes the algorithm more robust and, in fact, has been shown to be suitable for this case.

4.2 Square-section mesh

Even for the configuration with the squared cross-section, the domain, shown in figure 4.1, was modelled parametrically with respect to the reference length, which in this case is the side of the square *L*. The overall size of the domain is 55L in length and 30L in height. The square section has its center positioned 15L apart from the inlet; it is surrounded by a square area that measures 9L on the side and corresponds, similarly to the cylinder case, to the area of the dynamic mesh, i.e., within which the mesh fits to follow the movements of the square.

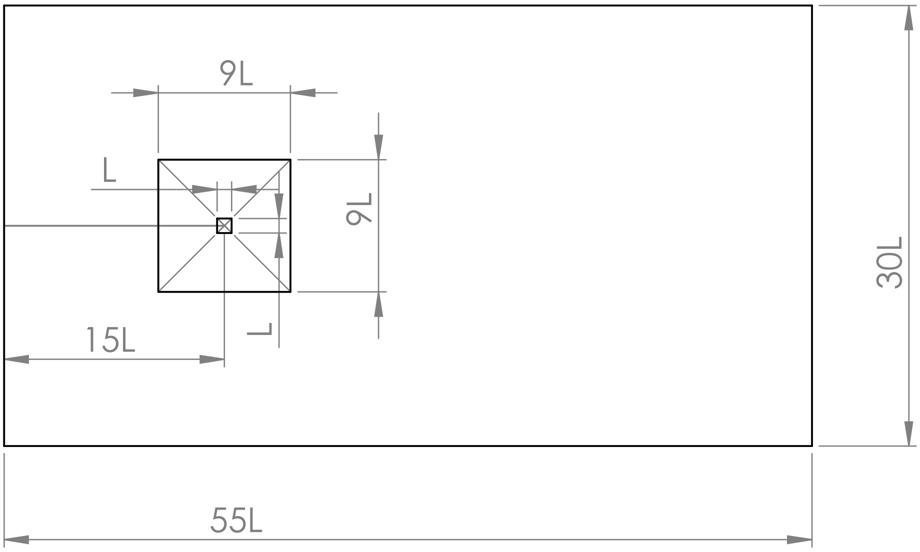

Figure 4.1: *Domain geometry with parametric dimensions in function of the square side L*

A sensitivity study also extensively tested the mesh used for the square-section case. In fact, three meshes of different resolutions were tested in this case as well. The coarsest mesh has approximately 25K elements, the medium-resolution mesh has approximately 50K elements, and the most refined mesh has approximately 95K elements. Simulations were run for each of these meshes by adopting three different turbulence models. These simulations computed the values of drag coefficients, pressure coefficients and skin friction coefficients. The results were then compared to identify the best mesh for this case. The results obtained were also compared with the information available in the literature; in particular, the values of the drag coefficient were compared with what results from the DNS (Direct-Navier-Stokes) of Trias et al. (2015). The values obtained from the RANS simulations with the meshes agree with what was calculated by Trias; the variation in results between the three meshes is minimal. The pressure coefficient values were also compared with the results obtained by Cao and Tamura (2016) and Bearman and Obasaju (1982); again, the values are in agreement.

Regarding the turbulence models tested, as in the cylinder case, the Spalart-Allmaras, $k-\omega$-SST and Transition-SST were used. For all the parameters tested, these showed no significant differences between the various simulations.

Therefore, the mesh adopted is the coarsest among the proposals, and although the Salart-Allmaras turbulence model also gave good results, the $k\omega$-SST was chosen as the turbulence model.
Finally, the value of $y+$ along the entire perimeter of the square profile was calculated to check the mesh's ability to capture the boundary layer correctly. The values that were obtained turned out to be less than one everywhere for both the steady and unsteady cases tested.

Again, a hybrid mesh was used, as can be seen in figure 4.2, composed of triangular and quadrangular elements in an O-grid configuration.
The inflation layer, figure 4.2c, is arranged around the square to capture the fluid wall behaviour correctly. Note that the corners of the square are not right angles but have been rounded, as can be seen in figure 4.2b, with a fillet radius of length 0.01L in order to avoid edges, which, by going to affect the skewness of the elements, considerably deteriorate the quality of the mesh. Finally, one can see the thickening of the mesh in the areas of interest, namely the area surrounding the square and the wake area.

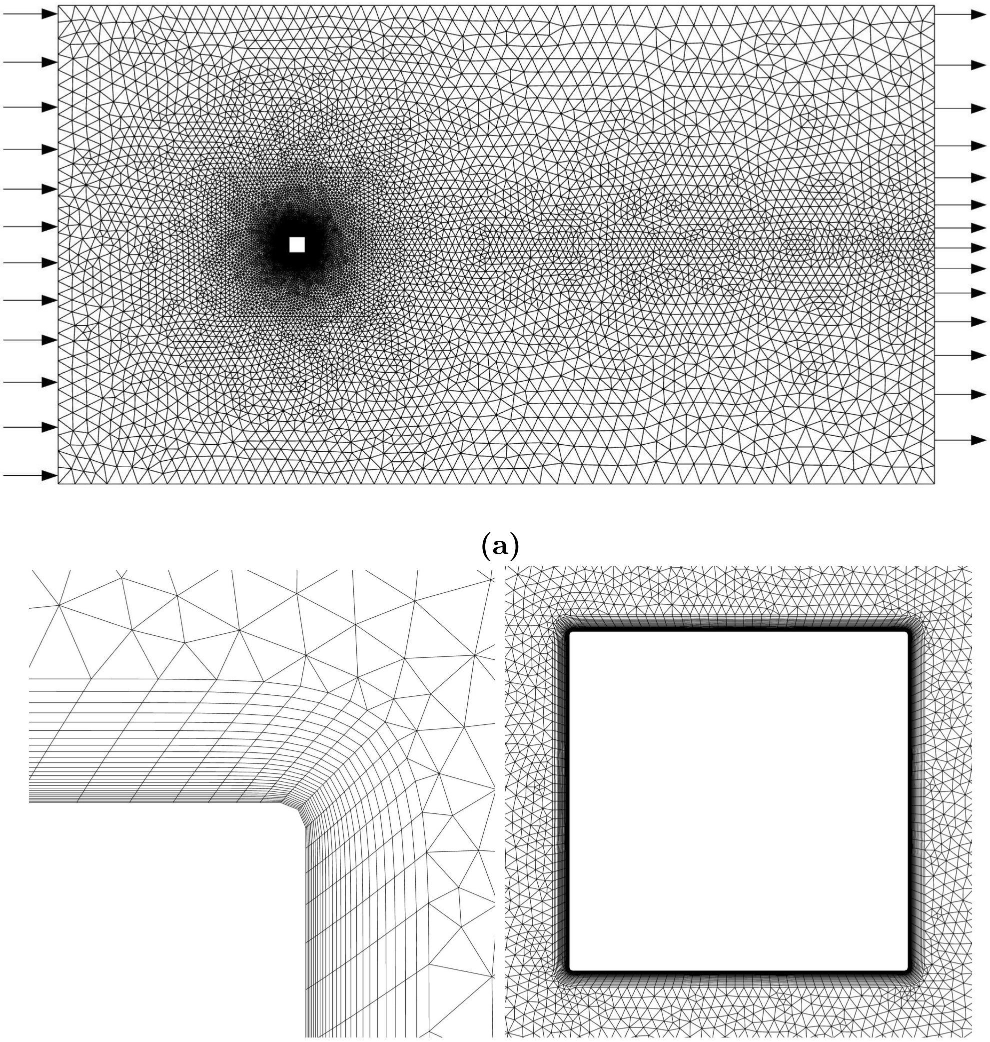

(a)

(b) **(c)**

Figure 4.2: *Full fluid domain (**a**); square wall zone (**b**); focus on the square section (**c**).*

4.3 Dynamic analysis

As in the cylindrical case, the simulations for the square case were divided into two main groups at constant xi and at constant k^*, evaluating for each the oscillation frequency via the Stourhal number, the amplitude of the oscillations and the non-dimensional mechanical power produced.

However, a few remarks should be made before presenting the data obtained. The configuration with the square cross-section was chosen because it is expected to have large oscillations for larger values of U_r than the case with the circular cross-section. This is because the expected frequency of vortex detachment is higher than in the cylinder case. Trias et al. (2015) suggests values of St around 0.13 and, recalling the definition of the Stourhal number in our case, these would correspond to relative velocity values of approximately $U_r = 8$ in the lock-in zone.

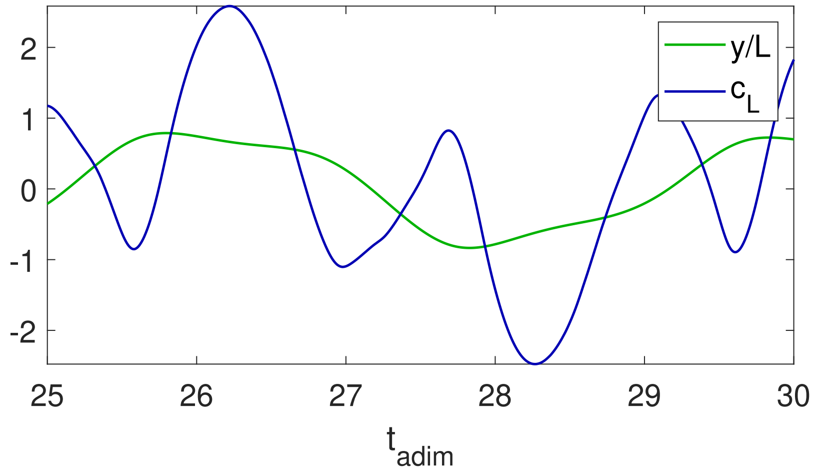

Figure 4.3: *Lift coefficient and normalized displacement vs. non-dimentional time;* $U_r = 14$ $k^* = 0.5$.

However, as it turns out, the lock-in condition never seems to occur for this configuration. The graph 4.3 is shown here to highlight how the lift coefficient is characterised by a higher oscillation frequency compared to that of the body. This underlines the fact that the lock-in condition does not exist, as the square body does not follow the primary vortex that is responsible for the lift force that the fluid applies on the body. As will be discussed later, the frequency analysis of the simulated cases confirms the absence of the lock-in condition for practically all simulated velocities.

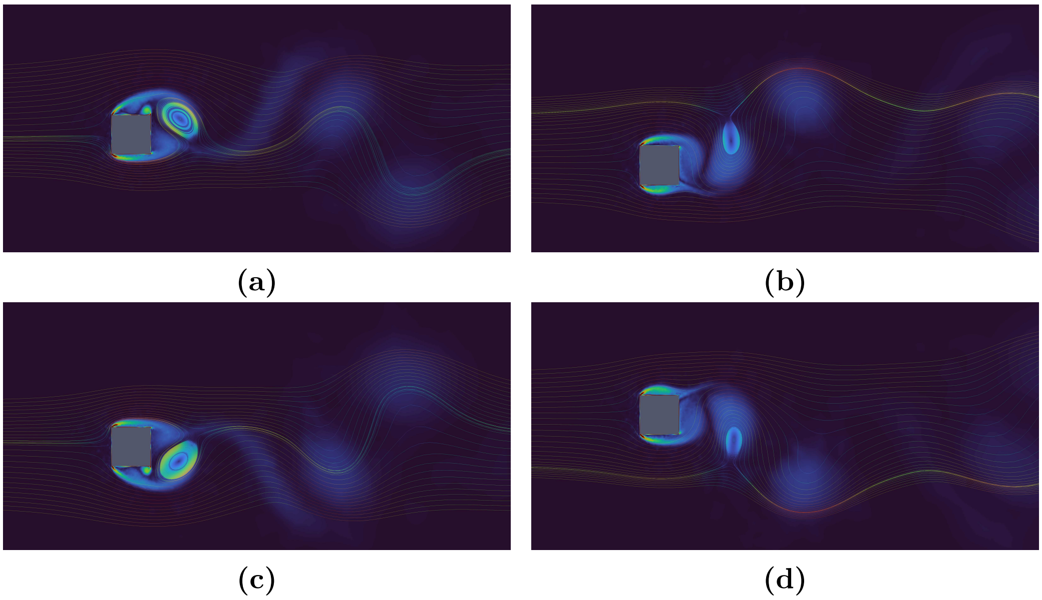

Figure 4.4: *Velocity field streamlines and vorticity magnitude contour for an oscillating square body.*

The same conclusion can be drawn by looking at figure 4.4, where streamlines and vorticity magnitude are plotted. It can be seen that the cylinder and the downstream primary vortex are not synchronised, which is at odds with the vortex-shedding vibration pattern that was intended to be exploited.

Another point to be noted is that, unlike in the case of the cylinder, the Stourhal number is not necessarily constant as Reynolds varies; however, in this study, the assumption of constancy of St is maintained for the Reynolds range of the simulations from 10^4 to 10^5.

4.3.1 Constant ξ cases

Once again, it is recalled that this case is of mainly theoretical interest due to the fact that the constancy of ξ imposes significant variations of ρ as the velocity varies. However, given the behaviour of the cylinder in the free case at constant ξ, which always resulted in the lock-in condition, it was decided to study the same configuration also for the square section case.
The values that were imposed on the variables in this set of simulations are as follows:

- $\xi = 9$
- $f_n = 0.1$
- $\zeta = 0.00,\ 0.05,\ 0.1$
- $U_r = 2.0 - 20.0$

The range of velocities for which the simulations were performed is at higher values than for the cylinder because, given the considerations made earlier regarding the typical Stourhal number for this case, the most interesting occurrences are expected at higher velocities, with values around $U_r = 8$.

With regard to the analysis of the oscillation frequencies, the trends of the curves are shown in figure 4.5 . Along with the points corresponding to the simulations results, the hyperbola indicating the frequencies for which the lock-in condition exists is also shown. The curves obtained approximate the lock-in curve but never consistently adhere to it. The observed behaviour is very different from the cylinder case; in fact, firstly, it can be observed that the purple curve, corresponding to the null value of the damping, does not adhere to the lock-in condition and, moreover, it has not very regular trend in the interval between $U_r = 4$ and $U_r = 6$. Furthermore, the increase in the damping ratio does not seem to have any effect on the behaviour of the body; the course of the curves remains almost unchanged compared to the free case, although it retains some irregularity. Part of this irregularity could be attributed to the imperfect convergence of some simulations; however, as the results are not particularly promising, the level of accuracy achieved was deemed sufficient. Finally, it can be noted that the values of the Sthoural number, excluding the lowest velocity values, assume relatively low values, lower than those suggested by Trias et al. (2015).

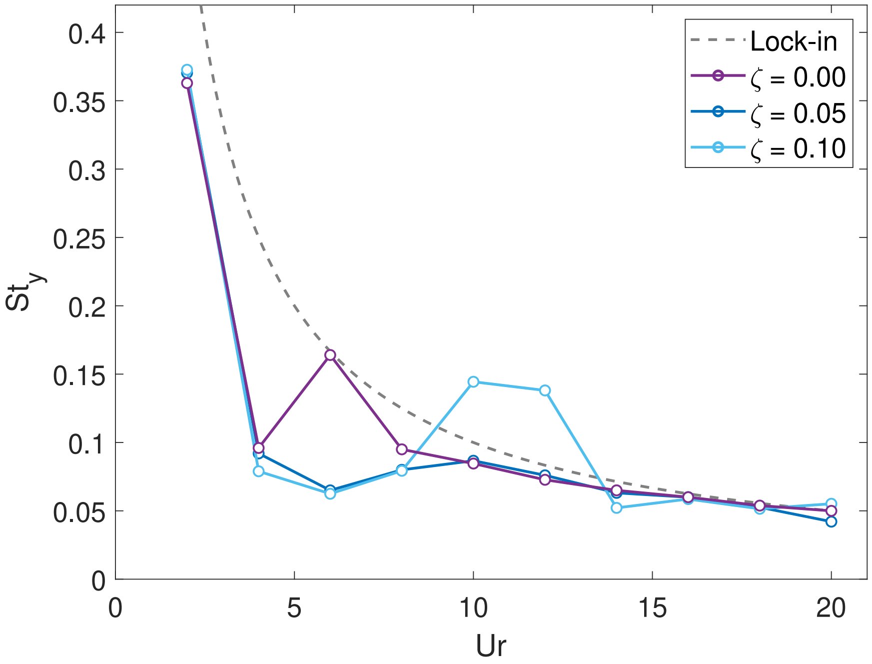

Figure 4.5: *The plot of the Strouhal number St_y versus velocity $Ur = U_\infty / f_n L$ for simulations at $\xi = 9$ and values of the damping ratio given in the legend.*

About the amplitude of the oscillations, the root mean square values of the displacements were also evaluated. The 4.6 graph shows the curve trends obtained from the simulations. A clear difference between the free and the damped case can be seen. The violet curve, with zero damping, always grows as U_r increases; this trend is in contrast to what one would expect from a vortex shedding-induced vibration, which has a bell-shaped trend, like that of the cylinder case. On the other hand, the increasing behaviour agrees with what Kaneko et al. (2008) reports for diverse types of flow-induced vibration for which vortices are formed differently, for example, by shedding from the forward corners of the square or by other phenomena that change the pressure field. The effect of damping with respect to the amplitude of oscillation in this configuration is drastic; curves with ζ values greater than zero show minimal amplitudes and a somewhat irregular pattern. The blue-coloured curve, representative of the maximum simulated damping, shows almost zero displacement over almost the entire range of simulated velocities.

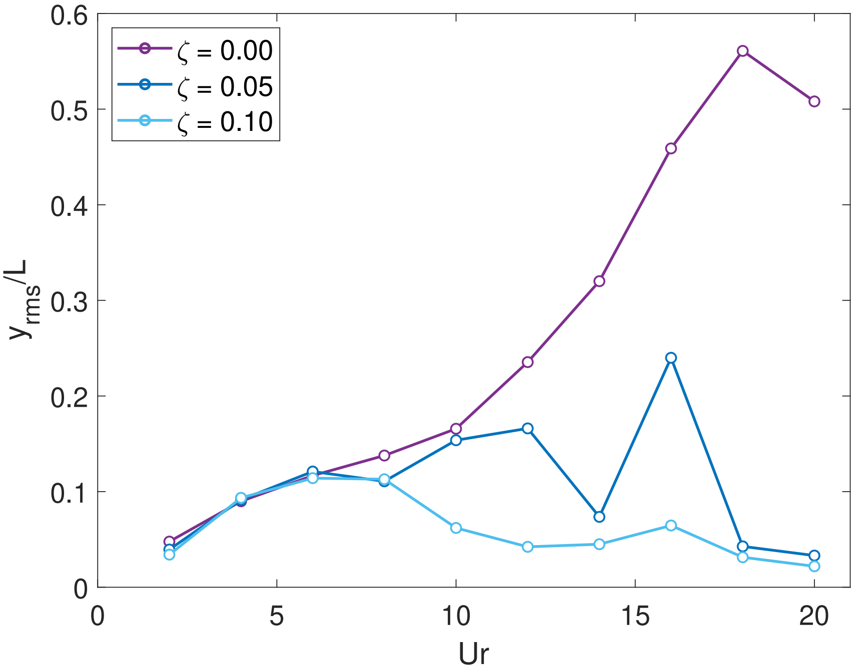

Figure 4.6: *The plot of the* y_{rms}/L *versus velocity* $Ur = U_\infty/f_n L$ *for simulations at* $\xi = 9$ *and values of the damping ratio given in the legend.*

Again, the dimensionless mechanical power P^* is evaluated as a parameter of interest, and it's calculated as follows:

$$P^*(t) = \frac{\dot{y}(t)}{U_\infty} \frac{F_y}{1/2\rho_\infty L U_\infty^2} \qquad 4.7$$

The results represented in the 4.7 graph reflect what has already been noted in the two previous graphs. The curve corresponding to the non-damped case presents the highest values of power produced at very high speeds; we note that in the interval between $U_r = 6$ and $U_r = 12$, P^* assumes almost constant values. On the other hand, the damped curves assume the highest values at lower speeds and then decrease to nearly zero. At one point, these seem to exceed the power values produced by the non-damped case, however, this irregularity is also due to the imperfect convergence of some simulations.
In general, the power values produced are relatively low when compared with

those produced by the cylinder in the same configuration; furthermore, their irregularity makes the case uninteresting from studying vortex shedding.

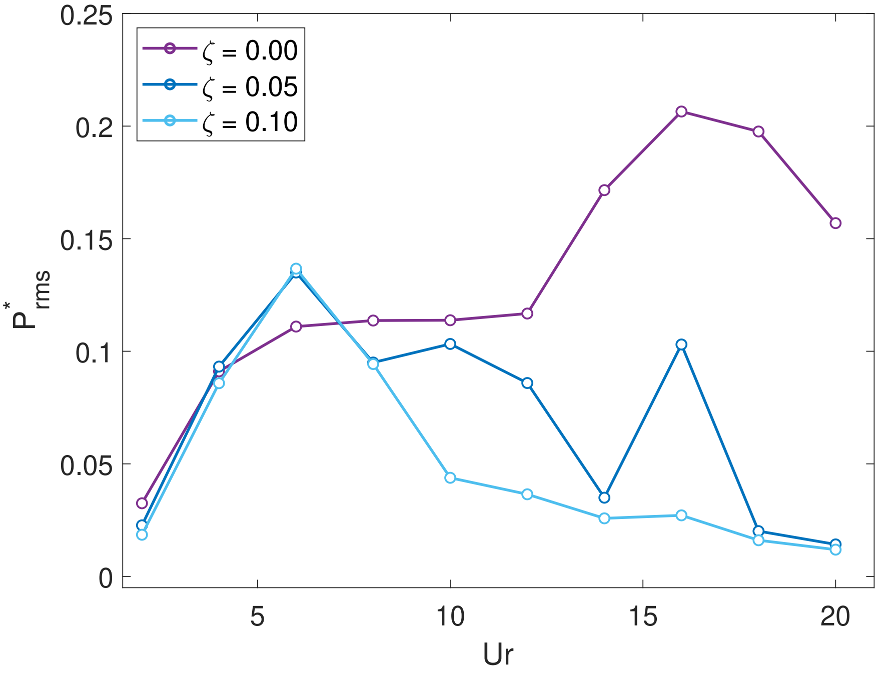

Figure 4.7: *The plot of the* P^*_{rms} *versus velocity* $Ur = U_\infty/f_n L$ *for simulations at* $\xi = 9$ *and values of the damping ratio given in the legend.*

4.3.2 Constant k^* cases

Moving on to the analysis of the simulations at constant k^*, remember that the constancy of k^* implies the constancy of k and allows the value of ρ to be imposed, so again, this set of analyses is of practical interest. In this set of simulations, relatively high values of the damping ratio ζ were also evaluated; this was done because we wanted to see if it was possible to make the operation of the device stable over a range of speeds, with the amplitude of the oscillations decreasing beyond certain values of U_r instead of increasing indefinitely.

The values set for this set of simulations are as follows:

- $k^* = 0.5$
- $\rho = 8$
- $\zeta = 0.1, 0.2, 0.3, 0.4$
- $U_r = 2.0 - 20.0$

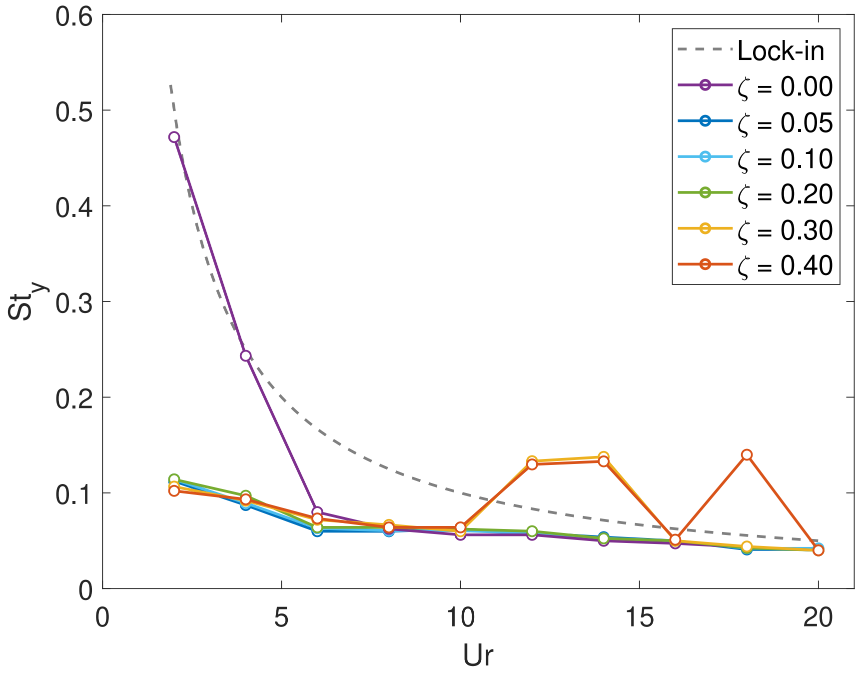

Figure 4.8: *The plot of the Strouhal number* St_y *versus velocity* $Ur = U_\infty / f_n L$ *for simulations at* $k^* = 0.5$ *and values of the damping ratio given in the legend.*

Regarding the frequency analysis, figure 4.8 shows that the lock-in condition is almost never reached in this configuration. Only the violet curve, at zero damping, seems to highlight a zone, at low values of U_r, in which the oscillations of the square body and the detachment frequency of the vortices are synchronous; for higher values of reduced velocity, the curve settles instead along with the others.

As far as the effect of damping on the system is concerned, there are no significant differences between the analysed cases. The trend shown by the curves indicates almost constant values as U_r changes, and these are not altered even by the intense increase in the damping ratio, which reaches the value of $\zeta = 0.4$. It should also be noted that the measured Stourhal number values are slightly lower than those measured by Trias et al. (2015), which vary between $St_y = 0.1 - 0.03$. This difference is mainly attributable to the difference in Reynolds number compared to the Trias case.

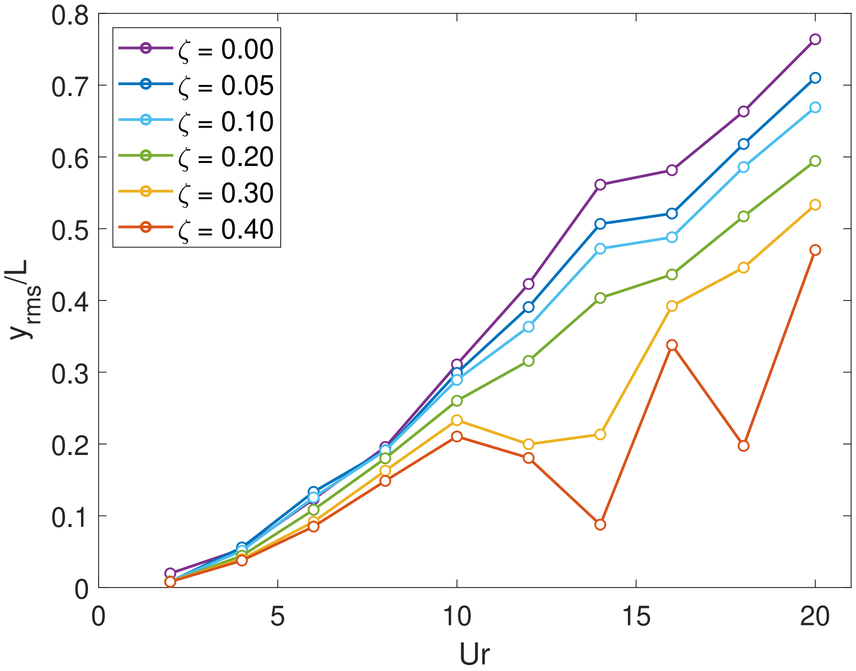

Figure 4.9: *The plot of the y_{rms}/L versus velocity $Ur = U_\infty/f_nL$ for simulations at $k^* = 0.5$ and values of the damping ratio given in the legend.*

Concerning the oscillations' amplitude, the root mean square values are evaluated once again. From the 4.9 graph, one can see the increasing and almost linear trend of the zero-damping case. This behaviour is typical of flow-induced vibrations not driven by vortex shedding and can instead be attributed to wind galloping in accordance with Kaneko et al. (2008). In this set of simulations, relatively high ζ values were imposed in order to obtain a lowering of the curve that would show a U_r regime where the operation of the device was stable, as was the case for the cylinder. However, it can be seen from the graph that this result was not achieved; increasing the damping ratio does indeed reduce the amplitude of the oscillations, which, however, always increase as U_r increases. Not even very high values of ζ give effective results in these terms, they tend instead to make the course of the curves very irregular and are not very exploitable for our purposes.

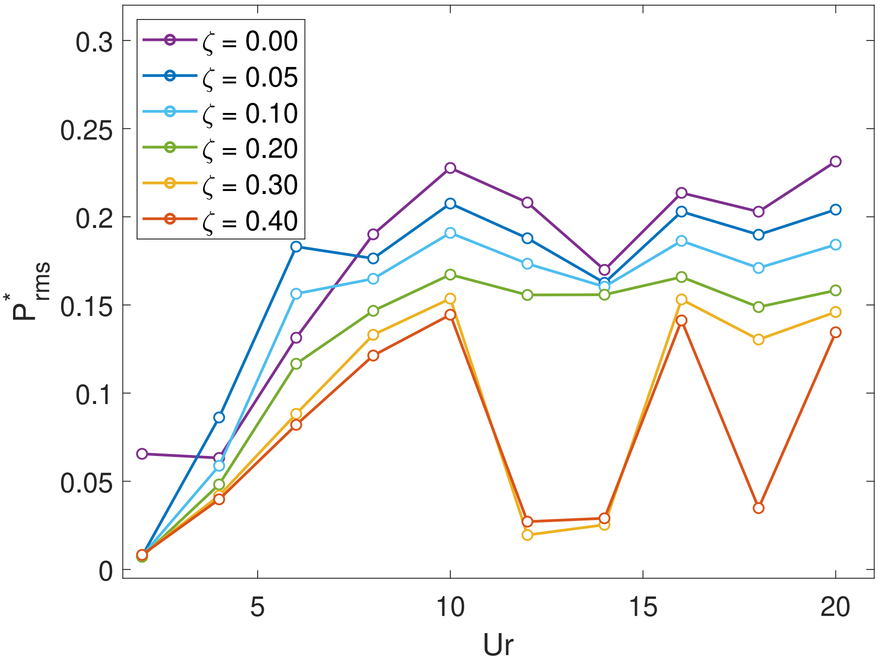

Figure 4.10: *The plot of the P^*_{rms} versus velocity $Ur = U_\infty/f_nL$ for simulations at $k^* = 0.5$ and values of the damping ratio given in the legend.*

As far as power is concerned, the dimensionless power P^* is also evaluated. The graph 4.10 shows an initial range of U_r, between 2 and 10, where the power generated grows proportionally with the flow velocity; for higher values instead, P^* seems to stabilise around 0.2 and remains more or less constant throughout the simulated velocity range.

The generated power decreases as the damping increases, maintaining the same trend as shown for the undamped curve. Excessive values of the damping ratio, $\zeta = 0.3 - 0.4$, once again make the curve trend uneven. Finally, it can be seen that the maximum values of P^* are obtained in the velocity range around $U_r = 10$, which is much greater than that found in the cylinder case, where the maximum peak was for $U_r = 3$.

In conclusion, some general observations can be made concerning the case with the square section. First of all, we highlight the fact that the best performance for this configuration occurs for higher values of U_r than for the cylinder case; this confirms the initial hypothesis and makes this configuration exploitable where flows have higher velocities. Regarding the power output, its constancy as U_r varies is appreciated; this characteristic could be helpful in conditions where the flow velocity undergoes significant variations. However, it must be noted that the square body presents less regular trends when compared with the cylinder and, in particular, lacks a range of velocities for which the operation is stable.

- V -

Conclusions

The objective of this study was to give guidelines, concerning mechanical damping, for the design of VIV energy harvesters. The information to be obtained was intended to be as general as possible in order to keep their field of applicability broad.

The configuration adopted for this research is the open stream, for which two different configurations were studied: the cylinder and the square-based prism. The model adopted has only one degree of freedom, and the simplicity of this configuration is in line with the objective of outlining general guidelines. It must also be said that, in general, this type of energy harvester has fields of applicability for which high reliability and low maintenance requirements are advisable, so simple configurations are to be preferred.

The two cases analysed gave very different results:

- The circular section case shows a wide range of velocities for which the vortices and body oscillations are synchronous, i.e. the lock-in condition exists. Of the two cases analysed for this configuration, the constant ξ configuration produced very interesting results; it shows that for an undamped system, the lock-in condition is maintained for any flow velocity while in the presence of damping, even with small ζ, the behaviour of the body changes radically. It would be necessary to conduct further studies at constant ξ to understand what phenomena extend the range of lock-in velocities so much in order to understand better why mechanical damping negates this condition. As far as the case of greatest application interest at constant k^* is concerned, this shows good behaviour of the cylinder as the damping varies. In fact, the lock-in area is not excessively altered by ζ, as is the amplitude of oscillation. The study of the power produced has shown that the cylinder configuration has a relatively narrow range of applicability and needs the correct flow velocity to produce significant amounts of energy.

- The study of the behaviour of the square-base prism has highlighted the fact that the body oscillates asynchronously with respect to the detachment of the vortices, unlike the cylinder. The lock-in condition is never achieved in this configuration, neither for simulations conducted at constant ξ nor those conducted at constant k^*. The simulations at constant k^*, which are of interest for the application, do, however, show certain characteristics that can make this configuration useful. The applicability range with the square cross-section is different from that of the circular cross-section, which may be useful in conditions with high flow velocity. Furthermore, the study of the power output shows that an energy harvester with this configuration can produce significant amounts of energy over a much wider speed range. This can be very useful where the flow velocity varies frequently.

BIBLIOGRAPHY

[1] E. Achenbach and E. Heinecke. On vortex shedding from smooth and rough cylinders in the range of Reynolds numbers 6×103 to 5×106. *Journal of Fluid Mechanics*, 109(12), 1981. ISSN 14697645. doi: 10.1017/S002211208100102X.

[2] R. Badhurshah, R. Bhardwaj, and A. Bhattacharya. Lock-in regimes for Vortex-Induced Vibrations of a cylinder attached to a bistable spring. *Journal of Fluids and Structures*, 91, 2019. ISSN 10958622. doi: 10.1016/j.jfluidstructs.2019.102697.

[3] P. W. Bearman and E. D. Obasaju. An experimental study of pressure fluctuations on fixed and oscillating square-section cylinders. *Journal of Fluid Mechanics*, 119, 1982. ISSN 14697645. doi: 10.1017/S0022112082001360.

[4] H. Blackburn and R. Henderson. Lock-in behavior in simulated vortex-induced vibration. *Experimental Thermal and Fluid Science*, 12(2), 1996. ISSN 08941777. doi: 10.1016/0894-1777(95)00093-3.

[5] Y. Cao and T. Tamura. Large-eddy simulations of flow past a square cylinder using structured and unstructured grids. *Computers and Fluids*, 137, 2016. ISSN 00457930. doi: 10.1016/j.compfluid.2016.07.013.

[6] Y. Constantinides and O. H. Oakley. Numerical prediction of bare and straked cylinder VIV. In *Proceedings of the International Conference on Offshore Mechanics and Arctic Engineering - OMAE*, volume 2006, 2006. doi: 10.1115/OMAE2006-92334.

[7] F. De Vanna, A. Benato, and G. Cavazzini. Preliminary design guidelines for a vortex-based energy harvester for water flows. In *36th International Conference on Efficiency, Cost, Optimization, Simulation and Environmental Impact of Energy Systems, ECOS 2023*, 2023. doi: 10.52202/069564-0052.

[8] Z. J. Ding, S. Balasubramanian, R. T. Lokken, and T. W. Yung. Lift and damping characteristics of bare and straked cylinders at riser scale Reynolds numbers. In *Proceedings of the Annual Offshore Technology Conference*, volume 1, 2004. doi: 10.4043/16341-ms.

[9] C. A. Friehe. Vortex shedding from cylinders at low Reynolds numbers. *Journal of Fluid Mechanics*, 100(2), 1980. ISSN 14697645. doi: 10.1017/S0022112080001127.

[10] S. Fu, J. Wang, R. Baarholm, J. Wu, and C. M. Larsen. Features of vortex-induced vibration in oscillatory flow. *Journal of Offshore Mechanics and Arctic Engineering*, 136(1), 2013. ISSN 1528896X. doi: 10.1115/1.4025759.

[11] I. Goswami, R. H. Scanlan, and N. P. Jones. Vortex-Induced Vibration of Circular Cylinders. I: Experimental Data. *Journal of Engineering Mechanics*, 119(11), 1993. ISSN 0733-9399. doi: 10.1061/(asce)0733-9399(1993)119:11(2270).

[12] O. M. Griffin. Vortex shedding from bluff bodies in a shear flow: A review. *Journal of Fluids Engineering, Transactions of the ASME*, 107(3), 1985. ISSN 1528901X. doi: 10.1115/1.3242481.

[13] E. Guilmineau and P. Queutey. A numerical simulation of vortex shedding from an oscillating circular cylinder. *Journal of Fluids and Structures*, 16(6), 2002. ISSN 08899746. doi: 10.1006/jfls.2002.0449.

[14] S. Kaneko, T. Nakamura, F. Inada, and M. Kato. *Flow induced vibrations: Classifications and lessons from practical experiences.* 2008. doi: 10.1016/B978-0-08-044954-8.X0001-0.

[15] F. R. Menter. Two-equation eddy-viscosity turbulence models for engineering applications. *AIAA Journal*, 32(8), 1994. ISSN 00011452. doi: 10.2514/3.12149.

[16] F. R. Menter, R. B. Langtry, S. R. Likki, Y. B. Suzen, P. G. Huang, and S. Völker. A correlation-based transition model using local variables - Part I: Model formulation. *Journal of Turbomachinery*, 128(3), 2006. ISSN 0889504X. doi: 10.1115/1.2184352.

[17] E. Molino-Minero-Re, M. Carbonell-Ventura, C. Fisac-Fuentes, A. Mànuel-Làzaro, and D. M. Toma. Piezoelectric energy harvesting from induced vortex in water flow. In *2012 IEEE I2MTC - International Instrumentation and Measurement Technology Conference, Proceedings*, 2012. doi: 10.1109/I2MTC.2012.6229686.

[18] M. S. Pantazopoulos. Vortex-induced vibration parameters: Critical review. In *Proceedings of the International Conference on Offshore Mechanics and Arctic Engineering - OMAE*, volume 1, 1994.

[19] M. Raissi, Z. Wang, M. S. Triantafyllou, and G. E. Karniadakis. Deep learning of vortex-induced vibrations. *Journal of Fluid Mechanics*, 861, 2019. ISSN 14697645. doi: 10.1017/jfm.2018.872.

[20] K. Singh, S. Michelin, and E. de Langre. Energy harvesting from axial fluid-elastic instabilities of a cylinder. *Journal of Fluids and Structures*, 30, 2012. ISSN 08899746. doi: 10.1016/j.jfluidstructs.2012.01.008.

[21] P. R. Spalart and S. R. Allmaras. One-equation turbulence model for aerodynamic flows. *Recherche aerospatiale*, (1), 1994. ISSN 00341223. doi: 10.2514/6.1992-439.

[22] G. S. Triantafyllou, M. S. Triantafyllou, and C. Chryssostomidis. On the formation of vortex streets behind stationary cylinders. *Journal of Fluid Mechanics*, 170, 1986. ISSN 14697645. doi: 10.1017/S0022112086000976.

[23] F. X. Trias, A. Gorobets, and A. Oliva. Turbulent flow around a square cylinder at Reynolds number 22,000: A DNS study. *Computers and Fluids*, 123, 2015. ISSN 00457930. doi: 10.1016/j.compfluid.2015.09.013.

[24] J. Wang, C. Zhang, M. Zhang, A. Abdelkefi, H. Yu, X. Ge, and H. Liu. Enhancing energy harvesting from flow-induced vibrations of a circular cylinder using a downstream rectangular plate: An experimental study. *International Journal of Mechanical Sciences*, 211, 2021. ISSN 00207403. doi: 10.1016/j.ijmecsci.2021.106781.

ACKNOWLEDGEMENTS

Un sentito ringraziamento al professor Francesco De Vanna per l'estrema disponibilità dimostrata nel seguirmi durante il corso di questo studio; ci tengo a ringraziare anche il resto del gruppo di lavoro e, in particolare, il dottor Marco Carraro per il supporto fornitomi in molte occasioni.

Infine, rivolgo un ringraziamento alla mia famiglia, agli amici e a tutti coloro che mi hanno supportato durante il mio percorso universitario.